

CMS Draft Analysis Note

The content of this note is intended for CMS internal use and distribution only

2015/06/30
Head Id: 287440
Archive Id: 292555:294780M
Archive Date: 2015/05/04
Archive Tag: trunk

Search for Lepton Flavour Violating Decays of the Higgs boson in the $H \rightarrow e\tau$ channel

Daniel Troendle, Peter Schleper, Annika Vanhoefer¹, Colin Jessop, Nathan Kellams, Fanbo Meng², Suvadeep Bose³, Maria Cepeda, Sridhara Dasu, Aaron Levine⁴, Vincenzo Chiochia, Tomas Hreus, Silvia Taroni⁵, and Mauro Verzetti⁶

¹ University of Hamburg

² University of Notre Dame

³ University of Nebraska Lincoln

⁴ University of Wisconsin-Madison

⁵ University of Zurich

⁶ University of Rochester

Abstract

A search for Lepton Flavour Violating (LFV) decays of the recently discovered Higgs Boson using 19.70 fb^{-1} of $\sqrt{s} = 8 \text{ TeV}$ data taken in 2012 using the $H \rightarrow e\tau_\mu$ and $H \rightarrow e\tau_{had}$ channels is described, where τ_μ and τ_{had} indicate τ decays to muons and hadrons, respectively. Indirect limits constrain the branching fraction to 13%. A dedicated search improves the expected limit by approximately an order of magnitude. It is the first dedicated search for LFV Higgs decays in this channel at the LHC.

This box is only visible in draft mode. Please make sure the values below make sense.

PDFAuthor: V. Chiochia, C. Jessop
PDFTitle: Search for Lepton Flavour Violating Decays of the Higgs boson in the e-tau channel
PDFSubject: CMS
PDFKeywords: CMS, physics, Higgs, flavour

Please also verify that the abstract does not use any user defined symbols

1 Contents

2	1	Motivations	2
3	2	Analysis overview	2
4	3	Collected and simulated datasets	3
5	3.1	Data	3
6	3.2	Signal model	3
7	3.3	Simulated samples	3
8	4	Event reconstruction	3
9	5	Event selection	5
10	5.1	Overview	5
11	5.2	Efficiency of the trigger selection	6
12	5.3	Preselection: $H \rightarrow e\tau_\mu$ candidates	10
13	5.4	Preselection: $H \rightarrow e\tau_{had}$ candidates	10
14	5.5	Signal discrimination	11
15	5.6	Event categories and final selection	12
16	6	Background estimates	15
17	6.1	Background estimates for $H \rightarrow e\tau_\mu$	15
18	6.2	Background estimates for $H \rightarrow e\tau_{had}$	19
19	7	Comparison of measured and expected distributions	25
20	7.1	$e\tau_\mu$ channel	25
21	7.2	$e\tau_{had}$ channel	25
22	8	Systematic errors	31
23	8.1	Nuisance parameters	31
24	8.2	Systematic uncertainties in the template shapes	32
25	9	Results	33
26	10	Exclusion limits on LFV Higgs Yukawa couplings	37
27	11	Conclusions	37
28	A	Control plots after preselection	44
29	A.1	$e\tau_{had}$ channel	44
30	A.2	$e\tau_\mu$ channel	47
31	A.3	$e\tau_\mu$ channel: shape systematics	50

32 1 Motivations

33 This analysis searches for non-standard model decays of the Higgs Boson as a signal of physics
 34 beyond the standard model. One such possibility is lepton flavour violating (LFV) decays.
 35 In 1976, Bjorken and Weinberg [1] were the first to observe that LFV decays were possible in
 36 $SU(2) \otimes U(1)$ gauge theories with more than one Higgs doublet. This allows the possibility
 37 of flavour violating transitions such as $\mu \rightarrow e$ mediated by scalar Higgs Bosons. It has led to
 38 extensive experimental searches for LFV transitions that are ongoing. No LFV transitions have
 39 been observed to date.

40 The observation of the Higgs Boson offers the possibility of direct searches for LFV Higgs cou-
 41 plings. Blankenburg, Ellis and Isidori [2] recently re-interpreted the indirect constraints on LFV
 42 decays into constraints on LFV Higgs decays and found them to be quite weak; $B(H \rightarrow \mu\tau) <$
 43 $\mathcal{O}(0.1)$, $B(H \rightarrow e\tau) < \mathcal{O}(0.1)$. Harnik, Kopp and Zupan refined these limits further [3] and
 44 even re-interpretted ATLAS $H \rightarrow \tau\tau$ search results in terms of LFV decays to set more stringent
 45 limits. The possibility of LFV in Higgs decays up to about 10% of the rate motivates a dedicated
 46 search in CMS data. The search for the LFV decay $H \rightarrow \mu\tau$ was recently performed at CMS
 47 yielding an upper limit (95% CL) on the branching ratio of 1.87%, which is the most stringent
 48 limit to date in this channel. A slight excess of events (2.5σ) was observed with respect to the
 49 sum of SM signal and background predictions. This observation further supports the need for
 50 investigating an alternative decay channel, such as the $e\tau$ final state.

51 2 Analysis overview

52 A search for a LFV Higgs decay of a Higgs with $M_H = 125$ GeV in two channels $H \rightarrow e\tau_\mu$ and
 53 $H \rightarrow e\tau_{had}$ is performed, where τ_{had} and τ_μ are taus reconstructed in the hadronic and muonic
 54 τ decay channels, respectively. The 2012 dataset is used, corresponding to about 19.7 fb^{-1} col-
 55 lected at $\sqrt{s} = 8$ TeV. The final state signature is very similar to the standard model $H \rightarrow \tau_e\tau_{had}$,
 56 $H \rightarrow \tau_e\tau_\mu$ searches but with significant kinematic differences. The electron comes promptly
 57 from the LFV Higgs decay and tends to have a larger momentum than in the SM case as dis-
 58 cussed in Ref. [4]. In addition, as the neutrinos in the decay arise from one tau which is heavily
 59 boosted, they tend to be collinear with the visible tau decay products.

60 The similarity in the signature between LFV and SM $H \rightarrow \tau\tau$ decays means that the significant
 61 backgrounds are the same. In the case of $H \rightarrow e\tau_\mu$ the dominant background is $Z \rightarrow \tau_e\tau_\mu$.
 62 Other much smaller backgrounds come from jets faking leptons in $W + \text{jets}$, QCD multi-jets and
 63 $t\bar{t} + \text{jets}$ events. In the $H \rightarrow e\tau_{had}$ the dominant background is from jets faking taus in $W + \text{jets}$
 64 and QCD multi-jets. Less significant backgrounds also come from $Z \rightarrow \tau\tau$, $Z + \text{jets}$ and $t\bar{t} + \text{jets}$.
 65 The similarity to the SM $H \rightarrow \tau\tau$ analysis means much of the same analysis techniques and
 66 machinery that has already been employed successfully [5, 6] can be used. In particular, the
 67 tau leptons are reconstructed using the particle flow technique with the “hadrons plus strips”
 68 (HPS) and tau decay mode finding algorithms [7]. Particle flow muons, electrons, jets and E_T^{miss}
 69 are employed [8]. Furthermore, the analysis is very similar to our previous search for $H \rightarrow \mu\tau$
 70 decays, which is well documented in an analysis note [9], PAS [10], and paper [11]. The two
 71 channels are divided into categories based on the number of jets to enhance the sensitivity to
 72 the different Higgs production mechanisms, and the principle backgrounds are estimated with
 73 data driven methods. The presence or absence of signal is established using the asymptotic
 74 CL_s technique in which templates for signal and background are used to construct a binned
 75 likelihood function. The physical observable used to separate signal from background is the
 76 invariant mass of the final state leptons in the collinear approximation, which assumes the

⁷⁷ missing energy from neutrinos to be parallel to the visible tau decay products.

⁷⁸ 3 Collected and simulated datasets

⁷⁹ 3.1 Data

The January 22 2012 re-reco dataset with triggers given in table 1 is used.

Table 1: Triggers used in this analysis

Channel	Triggers
$H \rightarrow e\tau_\mu$	HLT_Mu8_Ele17_CaloIdT_CaloIsoVL_TrkIdVL_TrkIsoVL
$H \rightarrow e\tau_{had}$	HLT_Ele27_WP80

⁸⁰

⁸¹ 3.2 Signal model

⁸² The data are compared to the expectation based on theoretical calculations by the means of
⁸³ Monte Carlo simulations for signal and background processes. For the signal, the main SM
⁸⁴ production processes of gluon-gluon fusion and vector-boson fusion are taken into account. In
⁸⁵ this analysis, the LFV decays $H \rightarrow \mu\tau$, $H \rightarrow e\tau$ have been implemented in the latest version
⁸⁶ of PYTHIA 8.176 [12] running in CMSSW_5_3_13 with full detector simulation. From PYTHIA
⁸⁷ 8.150, the isotropic decay model of τ -leptons has been replaced with sophisticated τ -lepton
⁸⁸ decay machinery. This incorporates a full-modelled τ -lepton decay with spin correlation in-
⁸⁹ cluded and external packages such as Tauola are not needed to be accessed anymore. Further,
⁹⁰ from PYTHIA 8.170, the sophisticated τ decay machinery has been expanded so that it can also
⁹¹ handle production of τ 's in LFV processes, such as $H \rightarrow e^-\tau^+$. The dominant backgrounds,
⁹² which arise from vector boson production, are simulated with either MADGRAPH or PYTHIA.
⁹³ The full GEANT detector simulation is used for both signal and background samples.

⁹⁴ 3.3 Simulated samples

⁹⁵ The Monte Carlo datasets for signal and background processes used in this analysis are listed
⁹⁶ in Table 2. Corrections are applied for trigger efficiencies, electron and muon ID and isolation.
⁹⁷ Pileup re-weighting is also applied.

⁹⁸ 4 Event reconstruction

⁹⁹ A particle-flow (PF) algorithm [13–15] combines the information from all CMS subdetectors to
¹⁰⁰ identify and reconstruct the individual particles emerging from all vertices: charged hadrons,
¹⁰¹ neutral hadrons, photons, muons, and electrons. These particles are then used to reconstruct
¹⁰² the E_T^{miss} , jets, and hadronic τ decays, and to quantify the isolation of leptons and photons.

¹⁰³ The large number of proton interactions occurring per LHC bunch crossing (“pileup”), with an
¹⁰⁴ average of 9 in 2011 and 19 in 2012, makes the identification of the vertex corresponding to the
¹⁰⁵ hard-scattering process nontrivial, and affects most of the physics objects: jets, lepton isolation,
¹⁰⁶ etc. The tracking system is able to separate collision vertices as close as 0.5 mm along the beam
¹⁰⁷ direction [16]. For each vertex, the sum of the p_T^2 of all tracks associated with the vertex is
¹⁰⁸ computed. The vertex for which this quantity is the largest is assumed to correspond to the
¹⁰⁹ hard-scattering process, and is referred to as the primary vertex in the event reconstruction.

Table 2: Signal and background MC samples

Process	Name	Cross section (pb)
LFV Higgs Signal	LFV_GluGluHToTauE_M125_8TeV_Pythia8	19.27
	LFV_VBFHToTauE_M125_8TeV_Pythia8	1.58
SM Higgs	GluGluHToHToTauTau_M-125_8TeV-powheg-pythia6	19.27
	VBF_HToTauTau_M-125_8TeV-powheg-pythia6	1.58
$W \rightarrow l\nu + jets$	WJetsToLNu_TuneZ2Star_8TeV-madgraph +WXJetsToLNu_TuneZ2Star(X=1-4)	36257
$qq \rightarrow l^+l^- + jets$	DYJetsToLL_M50_TuneZ2Star_8TeVmadgraph +DYXJetsToLL_M50_TuneZ2Star_8TeVmadgraph	3503
$t\bar{t} + jets$	TTJets_FullLeptMGDecays_8TeVmadgraphtauola	26.20
	TTJets_SemiLeptMGDecays_8TeV-madgraphtauola	109.28
t,\bar{t}	/T(bar).tW-channel_TuneZ2star_8TeV-powheg-tauola	11.1 (11.1)
	T(bar).t-channel-DR_TuneZ2star_8TeVpowheg-tauola	56.4 (30.7)
$WW \rightarrow 2l2\nu + jets$	WWTo2L2Nu_TuneZ2star_8TeV_pythia6_tauola	5.824 (k-factor: 1.2)
$ZZ \rightarrow 4l$	ZZJetsTo4L_TuneZ2star_8TeV-madgraph-tauola	0.18
$ZZ \rightarrow 2l2Q$	ZZJetsTo2L2Q_TuneZ2star_8TeV-madgraph-tauola	2.502
$ZZ \rightarrow 2l2\nu$	ZZJetsTo2L2Nu_TuneZ2star_8TeV-madgraph-tauola	0.716
$WZ \rightarrow 2l2Q$	WZJetsTo2L2Q_TuneZ2star_8TeV-madgraph-tauola	2.21
$WZ \rightarrow 3l\nu$	WZJetsTo3LNu_TuneZ2_8TeV-madgraph-tauola	1.06
$W\gamma \rightarrow l\nu\gamma$	WGToLNuG_TuneZ2star_8TeV-madgraph-tauola	461.6
$W\gamma^* \rightarrow l\nu 2e$	WGstarToLNu2E_TuneZ2star_8TeV-madgraph-tauola	5.87 (k-factor: 1.5)
$W\gamma^* \rightarrow l\nu 2\mu$	WGstarToLNu2Mu_TuneZ2star_7TeV-madgraph-tauola	1.91 (k-factor: 1.5)
$W\gamma^* \rightarrow l\nu 2\tau$	WGstarToLNu2Tau_TuneZ2star_7TeV-madgraph-tauola	0.336 (k-factor: 1.5)

110 Jets are reconstructed from all the PF particles using the anti- k_T jet algorithm [17] implemented
 111 in FASTJET [18], with a distance parameter of $R = 0.5$. The jet energy is corrected for the contri-
 112 bution of particles created in pileup interactions and in the underlying event. This contribution
 113 is calculated as the product of the jet area and an event-by-event transverse momentum (p_T)
 114 density ρ , also obtained with FASTJET using all particles in the event. Charged hadrons, pho-
 115 tons, electrons, and muons reconstructed by the PF algorithm have a calibrated momentum or
 116 energy scale. A residual calibration factor is applied to the jet energy to account for imperfec-
 117 tions in the neutral-hadron calibration, the jet energy containment, and the estimation of the
 118 contributions from pileup and underlying-event particles. This factor, obtained from simula-
 119 tion, depends on the jet p_T and pseudorapidity η , and is on the order of 5% across the whole
 120 detector acceptance. Finally, a percent-level correction factor is applied to match the simulated
 121 jet energy response to the one observed. This correction factor and the jet energy scale uncer-
 122 tainty are extracted from a comparison between the observed data and simulation for γ +jets,
 123 Z+jets, and dijet events [19]. Particles from different pileup vertices can be clustered into a
 124 pileup jet, or significantly overlap a jet from the primary vertex below the p_T threshold applied
 125 in the analysis. Such jets are identified and removed using a boosted decision tree (BDT) [20]
 126 with the following input variables: momentum and spatial distribution of the jet particles,
 127 charged- and neutral-particle multiplicities, and compatibility of charged hadrons within the
 128 jet with the primary vertex. Jets originating from b-quark hadronization are identified using
 129 the combined secondary-vertex b-tagging algorithm [21].

130 Muons, electrons, and hadronically decaying τ leptons are reconstructed and identified as for
 131 the SM $H \rightarrow \tau\tau$ analysis [8].
 132 Hadronically decaying τ leptons are reconstructed and identified using an algorithm [22] which
 133 targets the main decay modes by selecting PF candidates with one charged hadron and up
 134 to two neutral pions, or with three charged hadrons. A photon from a neutral-pion decay
 135 can convert in the tracker material into an electron and a positron, which can then radiate
 136 bremsstrahlung photons. These particles give rise to several ECAL energy deposits at the same
 137 η value and separated in azimuthal angle, and are reconstructed as several photons by the PF
 138 algorithm. To increase the acceptance for such converted photons, the neutral pions are identi-
 139 fied by clustering the reconstructed photons in narrow strips along the azimuthal (ϕ) direction.
 140 To reconstruct electron candidates the track in the tracker is associated to the ECAL energy de-
 141 posit. The candidate is extract performing a Gaussian-sum-filter (GSF) fit to estimate the track
 142 parameter. The electrons are required to pass an identification variable based on a multivariate
 143 Boosted Decision Tree (BDT) discriminator based on track quality, cluster shape and kinematic
 144 quantities. The muon candidates are Tracker or Global muons, no isolation requirement are
 145 imposed, the track reconstructed in the tracker is required to be compatible with the track seg-
 146 ment in the muon detector, and the energy deposit in calorimeters has to be compatible with a
 147 muon as defined by a template based on the full detector simulation of the CMS detector.

148 5 Event selection

149 5.1 Overview

150 The event selection consists of several steps. First, a loose preselection is applied. The $H \rightarrow e\tau_\mu$
 151 sample is required to have an isolated electron and muon of opposite charge lying within the
 152 fiducial region of the detector while the $H \rightarrow e\tau_{had}$ is required to have isolated electron and
 153 hadronic tau of opposite charge. Particle flow objects [8] are used for muons and taus, while
 154 electron candidates are reconstructed with a MVA technique.

155 Next the signal variable, the collinear mass, is reconstructed and a signal window is defined.
 156 The events are then divided into three categories within each sample according to the number
 157 of jets in the event. This is designed to enhance the contribution of different Higgs production
 158 mechanisms. The zero jet category contains events primarily produced by gluon fusion. The
 159 one jet category contains events also produced by gluon fusion but also events produced in
 160 association with a W or Z boson decaying hadronically. The two jet category contains events
 161 produced by vector boson fusion.

162 Finally, in each category events are then selected by applying a set of event criteria. The event
 163 criteria are optimized to enhance the signal significance expected from simulated signal and
 164 background samples within the selected mass window.

165 The analysis was performed "blinded" in the region $100 \text{ GeV} < M_{\text{col}} < 150 \text{ GeV}$.

166 5.2 Efficiency of the trigger selection

167 The efficiency of the trigger selection is measured from data. For the $H \rightarrow e\tau_\mu$ channel, it is
 168 based on single-muon and single-electron datasets (reference triggers) listed in Table 3. The
 169 efficiency is calculated separately for muons and electrons from the ratio of the number of
 170 events firing the selection trigger (see Table 1) and the reference triggers divided by the number
 171 of events firing the reference trigger. The total trigger efficiency is given by the product of
 172 the muon and electron efficiencies, which are shown as a function of the lepton p_T and η , in
 Figure 1. The MC samples are rescaled by the measured efficiencies.

Table 3: Datasets and trigger slots used for trigger efficiency measurement

Dataset	Triggers
Single muon	HLT_IsoMu24_eta2p1 or HLT_IsoMu24
Single electron	HLT_Ele27_WP80

173

174 The $H \rightarrow e\tau_{\text{had}}$ data are selected using the single electron trigger reported in Table 1. The
 175 efficiency is measured from data with a tag and probe technique. The MC samples are rescaled
 176 by the measured efficiency, which is shown in Fig. 2. The trigger efficiency in bins of p_T and
 177 pseudorapidity is detailed in Table 4. The corresponding MC scale factors are listed in Table 5.

178

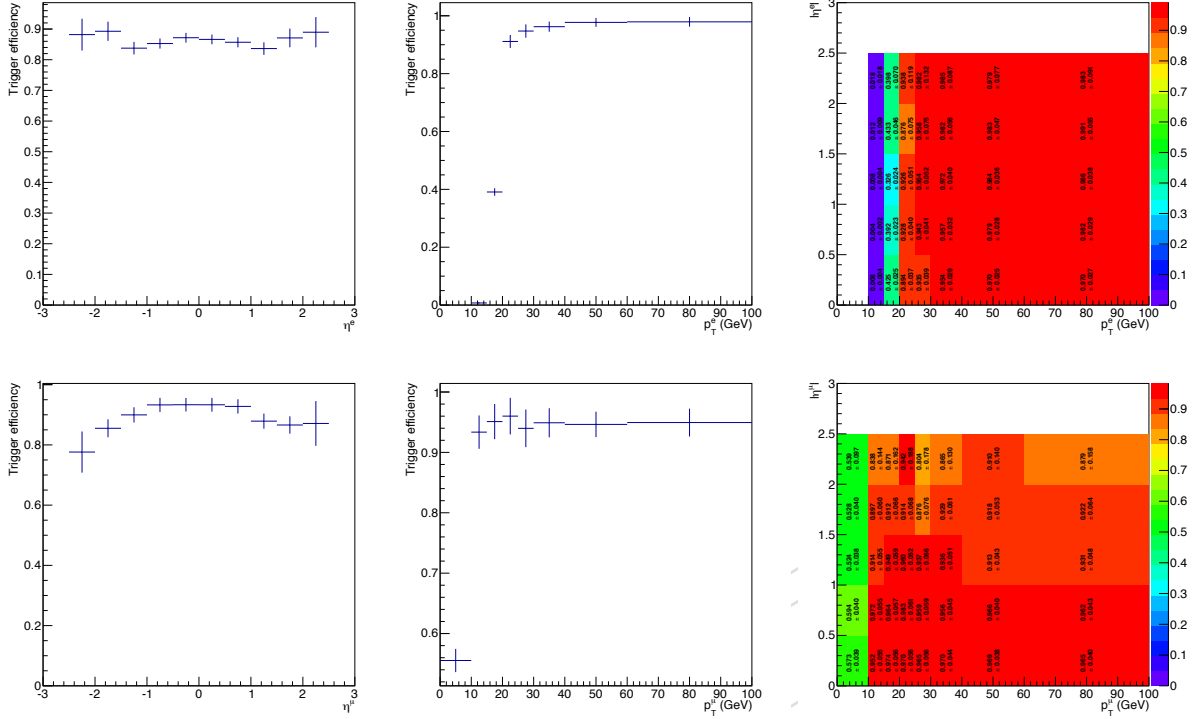


Figure 1: Trigger efficiencies of the $H \rightarrow e\tau_\mu$ channel for the electron (top) and muon (bottom) legs as a function of the lepton pseudorapidity (left), p_T (center) and both variables (right).

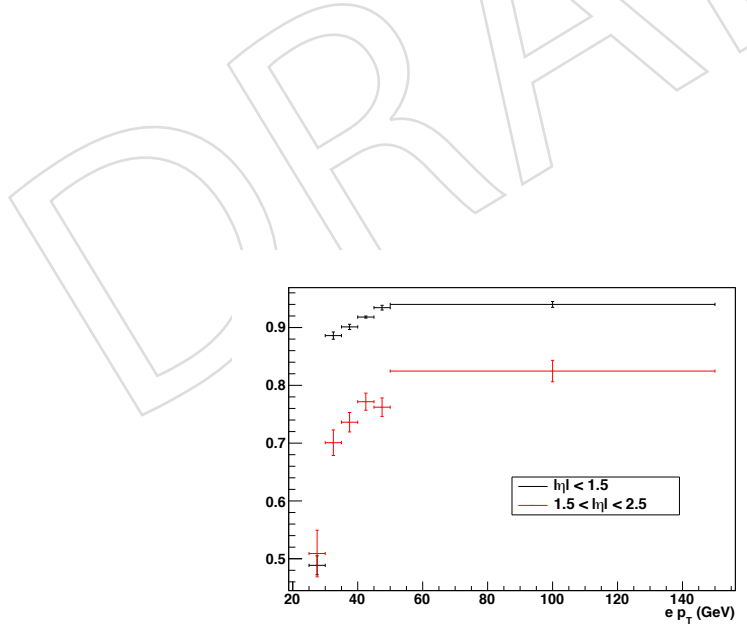


Figure 2: Trigger efficiencies of the $H \rightarrow e\tau_{had}$ channel as a function of the lepton p_T for the central (black) and forward (red) pseudorapidity regions.

Table 4: Trigger efficiency for the $e\tau_{had}$ channel.

min p_T	max p_T	min η	max η	Efficiency	Efficiency uncertainty
25.0	30.0	-2.5	-1.5	0.4559	0.0196
25.0	30.0	-1.5	0.0	0.4614	0.0166
25.0	30.0	0.0	1.5	0.4886	0.0164
25.0	30.0	1.5	2.5	0.5090	0.0403
30.0	35.0	-2.5	-1.5	0.7083	0.0647
30.0	35.0	-1.5	0.0	0.8689	0.0065
30.0	35.0	0.0	1.5	0.8860	0.0062
30.0	35.0	1.5	2.5	0.7007	0.0221
35.0	40.0	-2.5	-1.5	0.7620	0.0155
35.0	40.0	-1.5	0.0	0.8940	0.0045
35.0	40.0	0.0	1.5	0.9011	0.0045
35.0	40.0	1.5	2.5	0.7362	0.0168
40.0	45.0	-2.5	-1.5	0.7519	0.0142
40.0	45.0	-1.5	0.0	0.9236	0.0035
40.0	45.0	0.0	1.5	0.9181	0.0018
40.0	45.0	1.5	2.5	0.7717	0.0148
45.0	50.0	-2.5	-1.5	0.7568	0.0187
45.0	50.0	-1.5	0.0	0.9362	0.0043
45.0	50.0	0.0	1.5	0.9344	0.0041
45.0	50.0	1.5	2.5	0.7622	0.0160
50.0	7000.0	-2.5	-1.5	0.8117	0.0209
50.0	7000.0	-1.5	0.0	0.9463	0.0051
50.0	7000.0	0.0	1.5	0.9400	0.0050
50.0	7000.0	1.5	2.5	0.8247	0.0186

Table 5: MC scale factors for the trigger efficiency in the $e\tau_{had}$ channel.

min p_T	max p_T	min η	max η	scale factor (SF)	SF uncertainty
25.0	30.0	-2.5	-1.5	0.8065	0.0355
25.0	30.0	-1.5	0.0	0.5990	0.0216
25.0	30.0	0.0	1.5	0.6331	0.0213
25.0	30.0	1.5	2.5	0.9142	0.0729
30.0	35.0	-2.5	-1.5	1.0299	0.0942
30.0	35.0	-1.5	0.0	1.0091	0.0077
30.0	35.0	0.0	1.5	1.0280	0.0073
30.0	35.0	1.5	2.5	1.0261	0.0327
35.0	40.0	-2.5	-1.5	1.0663	0.0220
35.0	40.0	-1.5	0.0	1.0087	0.0051
35.0	40.0	0.0	1.5	1.0134	0.0051
35.0	40.0	1.5	2.5	1.0204	0.0235
40.0	45.0	-2.5	-1.5	1.0141	0.0193
40.0	45.0	-1.5	0.0	1.0213	0.0039
40.0	45.0	0.0	1.5	1.0130	0.0021
40.0	45.0	1.5	2.5	1.0297	0.0199
45.0	50.0	-2.5	-1.5	0.9898	0.0247
45.0	50.0	-1.5	0.0	1.0283	0.0048
45.0	50.0	0.0	1.5	1.0255	0.0046
45.0	50.0	1.5	2.5	0.9958	0.0211
50.0	7000.0	-2.5	-1.5	1.0515	0.0273
50.0	7000.0	-1.5	0.0	1.0271	0.0056
50.0	7000.0	0.0	1.5	1.0171	0.0055
50.0	7000.0	1.5	2.5	1.0544	0.0241

179 **5.3 Preselection: $H \rightarrow e\tau_\mu$ candidates**

180 The following criteria are applied at preselection level:

181 • **Electron**

- 182 • **ID:** loose MVA ID
- 183 • $p_T^e > 40 \text{ GeV}$, $|\eta|^e < 2.3$ excluding $1.4442 < |\eta| < 1.566$, $D_Z < 0.2$
- 184 • **Isolation:** $\text{RelPFIsoDB} < 0.10$
- 185 • **Conversion rejection**

186 • **Muon**

- 187 • **ID:** PFIDTight,
- 188 • $p_T^\mu > 10 \text{ GeV}$, $|\eta|^\mu < 2.1$, $D_z < 0.5$
- 189 • **Isolation:** $\text{RelPFIsoDB} < 0.12$

190 • **Missing Energy**

- 191 • Type-I corrected PFMET
- 192 • MET x,y shift correction applied

193 • **Further cuts**

- 194 • **Lepton charge:** muon and electron with opposite charge.
- 195 • $\Delta R_{e-\mu} > 0.1$
- 196 • $\Delta R_{e-jet} > 0.4$ for any jet with $p_T > 30 \text{ GeV}$
- 197 • $\Delta R_{\mu-jet} > 0.4$ for any jet with $p_T > 30 \text{ GeV}$
- 198 • **Veto:** extra PFIDTight muons with $p_T > 7 \text{ GeV}$
- 199 • **Veto:** extra loose MVA ID electrons with $p_T^e > 7 \text{ GeV}$
- 200 • **Veto:** no b-tagged (CSV medium wp) jet with $p_T > 30 \text{ GeV}$, $|\eta| < 2.4$.
- 201 • Visible mass $M_{vis} > 12 \text{ GeV}$

202 where (as detailed in [8]):

- 203 • **PFIDTight muons:** muons having the track in the tracker compatible with the track segment in the muon detector and the energy deposit in calorimeters compatible with a muons as defined by the template based on the full detector simulation of the CMS detector.
- 204 • loose MVA ID electrons: electrons identified requiring a BDT discriminator value above the *EGammaPOG* recommended value for the LooseID working point.
- 205 • **RelPFIsoDB:** the relative isolation of the candidate defined as

$$\text{RelPFIsoDB} = \frac{\Sigma p_T(\text{charged}) + \max(\Sigma E_T(\text{neutral}) + E_T(\text{photon}) - \Delta\beta, 0)}{p_T(\mu\text{ore})} \quad (1)$$

206 where $\Delta\beta$ corresponds to the energy estimate of neutral particles due to pile-up.

- 207 • **conversion rejection:** the electron track should have no missing hits in the inner layers of the pixel detector, no hits before the selected primary vertex and a vertex fit probability of more than $P > 10^{-6}$ to minimize the probability that the electron originates from a photon conversion.

214 **5.4 Preselection: $H \rightarrow e\tau_{had}$ candidates**

215 • **Electron**

- 216 • **ID:** MVA IDTight,

- 217 • $p_T^e > 30 \text{ GeV}$, $|\eta^e| < 2.3$ excluding $1.4442 < |\eta| < 1.566$, $D_z < 0.2 \text{ cm}$
 218 • **Isolation:** RelPFIsoDB<0.1
 219 • **Conversion rejection**
- 220 • **Tau**
- 221 • **ID:** PFTau (HPS) with tau DecayFinding.
 222 • $p_T^\tau > 30 \text{ GeV}$, $|\eta^\tau| < 2.3$, $dZ^\tau < 0.2$
 223 • **Isolation:** tightIsoHits3,
 224 • **Veto:** AntiElectronMVA5Tight or AntiMuon2Loose discriminator
- 225 • **Further cuts**
- 226 • **Veto:** no extra isolated electron (RelPFIsoDB<0.3) with $p_T > 10 \text{ GeV}$, no
 227 isolated muon with $p_T > 5 \text{ GeV}$, no extra taus with $p_T > 20 \text{ GeV}$ AntiElec-
 228 tronMVA5Tight and AntiMuon2Loose

229 • **Lepton charge** electron and tau with opposite charge.
 230 • $\Delta R_{\mu-jet} > 0.4$ for any jet with $p_T > 30 \text{ GeV}$
 231 • $\Delta R_{\tau-jet} > 0.4$ for any jet with $p_T > 30 \text{ GeV}$

232 where (ad detailed in [8]):

- 233 • loose MVA ID electrons: electrons identified requiring a BDT discriminator value
 234 above the *EGammaPOG* recommended value for the LooseID working point.
- 235 • PFTau (HPS) with tau DecayFinding: τ leptons decaying hadronically reconstructed
 236 with the PF algorithm combining charged hadron candidates and “ η - ϕ strips” in the
 237 calorimeter from the conversion of π^0 mesons.
- 238 • tightIsoHits3: the τ_{had} isolation is defined as

$$I_{\tau_{had}} = \sum p_T^{charged} (\Delta z < 2mm) + \max(p_T^\gamma - \Delta\beta, 0) \quad (2)$$

239 where Δz is the longitudinal impact parameter with respect to the τ_{had} production
 240 vertex. The tight working point is defined requiring the isolaiton p_T sum not to
 241 exceed 0.8 GeV.

- 242 • AntiMuon2Loose: the discriminator against muons working at the loose working
 243 point vetoes τ leptons in case a track segment in the muon system is found within a
 244 cone of size $\Delta R=0.5$ centered on the τ_{had} direction.
- 245 • AntiElectronMVA5Tight: the discriminator against electrons working at the loose
 246 working point vetoes τ lepton in case a electron candidate with MVA discriminator
 247 > -0.1 , out of the region $1.4442 < |\eta| < 1.566$ is found but there is no charged
 248 hadrons from the τ with a mass $< 0.55 \text{ GeV}$ and the energy deposit in calorimeter is
 249 less the 10% of the p_T of the track ($\text{EHCAL/Ptrack} < 0.1$) and 99% of the energy of
 250 reconstructec γ s is close to the leading PF candidate ($\Delta\eta < 0.03$)

250 5.5 Signal discrimination

251 The optimal signal discrimination variable is the one which best approximates the true mass
 252 of the Higgs particle. If both final state leptons in the Higgs decay can be fully reconstructed
 253 then this is the invariant mass of the two. However the neutrinos in the τ decay cannot be
 254 reconstructed and so some approximation of the Higgs mass must be used.

The first possibility is simply to use the invariant mass of the visible decay products, the visible
 255 mass M_{vis} . The second option is to use the collinear mass M_{col} . The collinear mass relies upon

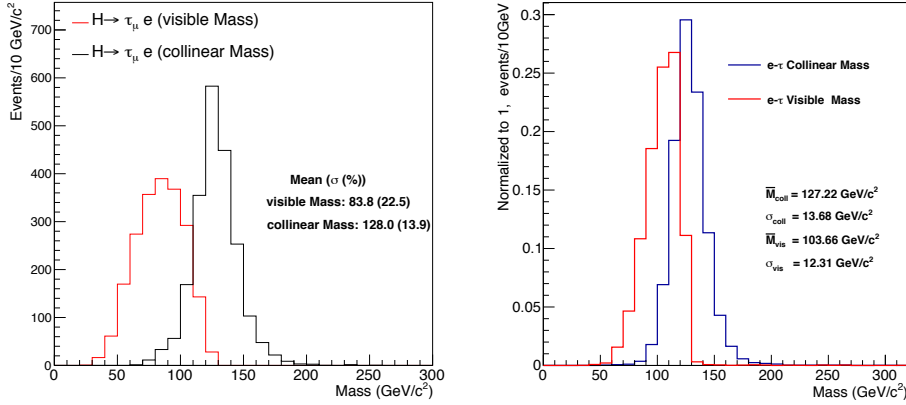


Figure 3: Visible mass M_{vis} and collinear mass M_{col} after preselection for the $H \rightarrow e\tau_\mu$ channel and 0-jet category (left), and for the $H \rightarrow e\tau_{\text{had}}$ channel and 2-jet category (right).

the collinear approximation [23]. Since the mass of the Higgs is much greater than the τ mass, the τ decay products are highly boosted in the direction of the original τ . Thus, the neutrino momenta can be approximated to be in the same direction as the other visible decay products of the τ . Hence the component of the missing transverse energy in the direction of the visible τ decay products is used to estimate the transverse component of the neutrino momentum:

$$\vec{p}_T^\nu = \vec{E}_T^{\text{miss}} \cdot \hat{p}_T^{\tau_{\text{vis}}} . \quad (3)$$

The fraction of the τ momentum carried by the visible τ decay products, $x_{\tau_{\text{vis}}}$, is then

$$x_{\tau_{\text{vis}}} = \frac{|\vec{p}_T^{\tau_{\text{vis}}}|}{|\vec{p}_T^{\tau_{\text{vis}}}| + |\vec{p}_T^\nu|} . \quad (4)$$

The τ four momentum is then $(x_{\tau_{\text{vis}}} |\vec{p}^{\tau_{\text{vis}}}|, x_{\tau_{\text{vis}}} \vec{p}^{\tau_{\text{vis}}})$ and since $M_H \gg m_\tau^2, m_l^2$:

$$M_H = M_{\text{col}} = \frac{M_{\text{vis}}}{\sqrt{x_{\tau_{\text{vis}}}}} . \quad (5)$$

Figure 3 shows a comparison of the visible mass and the collinear mass to illustrate the improvement gained by using the collinear approximation. Figure 4 shows M_{col} for signal and background after preselection for each category in each channel.

5.6 Event categories and final selection

The dataset is divided into three categories according to the number of jets in the event: 0-jet, 1-jet, and 2-jet category.

A set of kinematic variables is defined and criteria for selection are determined for each category and channel. For the $H \rightarrow e\tau_\mu$ channel, these criteria are optimized for significance $S/\sqrt{S+B}$, where S and B are the expected signal and background event yields from Monte Carlo samples in the mass window $100 \text{ GeV} < M_{\text{col}} < 150 \text{ GeV}$. For the $H \rightarrow e\tau_{\text{had}}$ channel, the event selection criteria are optimized for best expected significance in the mass window obtained from the official CMS combination tool [24] using simulated samples only and cross checking the result with the ratio $S/\sqrt{S+B}$. The signal strength is set according to the standard

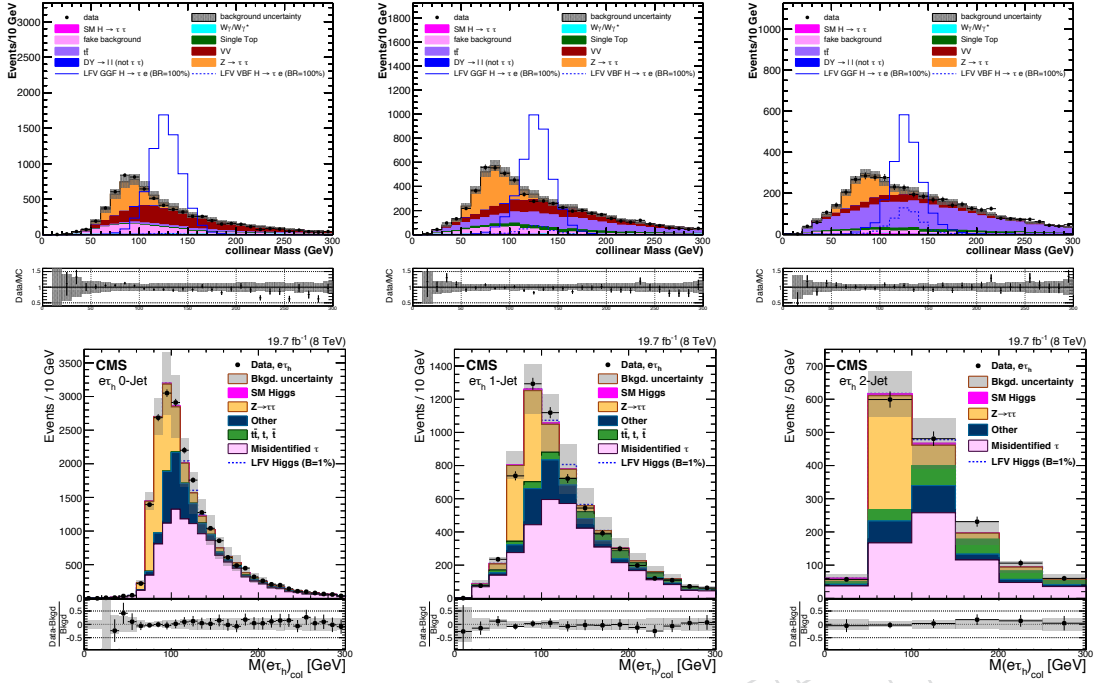


Figure 4: M_{col} after preselection for the $H \rightarrow e\tau_\mu$ (up) and $H \rightarrow e\tau_{had}$ channel (down) for the 0 (left), 1 (center) and 2-jet (right) category.

model Higgs production cross-section at $M_H = 125$ GeV with $B(H \rightarrow e\tau) = 1\%$. The analysis was performed “blinded” in the region $100 \text{ GeV} < M_{col} < 150 \text{ GeV}$.

The variables and the cut values are listed in Table 6 and 7 for the $H \rightarrow e\tau_\mu$ and $H \rightarrow e\tau_{had}$ channels, respectively. The measured and expected kinematic distributions after preselection are shown in the Appendix.

Table 6: Selection criteria for each event category after cut optimization, for the $H \rightarrow e\tau_\mu$ channel

0-jet category
<ul style="list-style-type: none"> • $p_T^e > 50 \text{ GeV}$ • $p_T^\mu > 15 \text{ GeV}$ • $\Delta\Phi(\mu, E_T^{\text{miss}}) < 0.8$ • No jets with $p_T^{\text{jet}} > 30 \text{ GeV}, \eta < 4.7$, LooseID
1-jet category
<ul style="list-style-type: none"> • $p_T^e > 40 \text{ GeV}$ • $p_T^\mu > 15 \text{ GeV}$ • $\Delta\Phi(\mu, E_T^{\text{miss}}) < 0.8$ • $\Delta\Phi(\mu, e) > 0.5$ • $m_T(\mu, E_T^{\text{miss}}) < 30 \text{ GeV}$ • One jet with $p_T^{\text{jet}} > 30 \text{ GeV}, \eta < 4.7$, LooseID
2-jet category
<ul style="list-style-type: none"> • $p_T^e > 40 \text{ GeV}$ • $p_T^\mu > 15 \text{ GeV}$ • $m_T(\mu, E_T^{\text{miss}}) < 40 \text{ GeV}$ • $p_T^{\text{jet}1} > 30 \text{ GeV}, p_T^{\text{jet}2} > 30 \text{ GeV}, \eta_{\text{jet}1} < 4.7, \eta_{\text{jet}2} < 4.7$, LooseID • $\Delta\eta(\text{jet}1, \text{jet}2) > 3$ • $M_{\text{jet}1-\text{jet}2} > 200 \text{ GeV}$

Table 7: Selection criteria for each event category after cut optimization, for the $H \rightarrow e\tau_{had}$ channel

0-jet category
<ul style="list-style-type: none"> • $p_{Te} > 45 \text{ GeV}, p_{T\tau} > 30 \text{ GeV}, \Delta\phi_{e\tau} > 2.3$ • $M_T(\tau) < 70 \text{ GeV}$ • No jets with $p_T^{\text{jet}} > 30 \text{ GeV}, \eta < 4.7$, LooseID
1-jet category
<ul style="list-style-type: none"> • $p_{Te} > 35 \text{ GeV}, p_{T\tau} > 40 \text{ GeV}$ • $M_T(\tau) < 40 \text{ GeV}$ • One jet with $p_T^{\text{jet}} > 30 \text{ GeV}, \eta < 4.7$, LooseID
2-jet category
<ul style="list-style-type: none"> • $p_{Te} > 35 \text{ GeV}, p_{T\tau} > 30 \text{ GeV}$ • $M_T(\tau) < 50 \text{ GeV}$ • $p_T^{\text{jet}1} > 30 \text{ GeV}, p_T^{\text{jet}2} > 30 \text{ GeV}, \eta_{\text{jet}1} < 4.7, \eta_{\text{jet}2} < 4.7$, LooseID • $\Delta\eta(\text{jet}1, \text{jet}2) > 2.3$ • $M_{\text{jet}1-\text{jet}2} > 400 \text{ GeV}$ • No jets with $p_T^{\text{jet}} > 30 \text{ GeV}$ with $\eta_{\text{jets}1} < \eta_{\text{jet}} < \eta_{\text{jet}2}$

273 6 Background estimates

274 The dominant backgrounds are estimated with data driven techniques while the less significant backgrounds are estimated with Monte Carlo simulations. The largest background in the
 275 $H \rightarrow e\tau_e$ channel is $Z \rightarrow \tau\tau$. It is evaluated using an embedding technique [25]. The next most
 276 significant background comes from $W + \text{jets}$ and a data driven method to estimate the misiden-
 277 tified leptons is used for this. In the $H \rightarrow e\tau_{had}$ channel the dominant $W + \text{jets}$ background is
 278 estimated using the same technique and, similarly, the second most significant background
 279 $Z \rightarrow \tau\tau$ uses the embedding technique. This method is employed slightly differently in both
 280 channels.

282 6.1 Background estimates for $H \rightarrow e\tau_\mu$

283 6.1.1 W+jets and other sources of misidentified leptons

284 The $W + \text{jets}$ process is an important background in the $H \rightarrow e\tau_\mu$ channel when the W decays
 285 to either an electron or muon and an additional so called misidentified lepton is present in the
 286 event. Misidentified leptons can be misidentified objects or real leptons produced in a hadronic
 287 jet. QCD multijet events with two such misidentified leptons can also enter the signal region.
 288 Other minor backgrounds involving misidentified leptons are $t\bar{t}$ events, where one top quark
 289 decays via a W boson into a lepton and a neutrino, whereas the other decays hadronically. This
 290 background is strongly suppressed due to a veto on b-tagged jets.

291 All processes involving misidentified leptons are predicted using a data driven method, where
 292 one measures the probability for an object with a loose set of requirements to pass predefined
 293 tight requirements. In the $H \rightarrow e\tau_\mu$ channel only misidentified muons have to be considered,
 294 since a high threshold on the electron transverse momentum of 40 GeV is set already at the
 295 preselection level and the misidentified electron contribution is assumed to be negligible. This
 296 can be seen in Figure 5, where the misidentified electron and muon composition is shown
 297 in the isolation sidebands, where one of the leptons is non-isolated. Non-isolated muons are
 298 defined similar to isolated muons (see section 5.3), but with inverted isolation requirement:
 299 $0.12 < \text{RelPFIsoDB} < 1.0$. Non-isolated electrons are defined similarly with different isolation
 300 criteria: $0.1 < \text{RelPFIsoDB} < 0.2$.

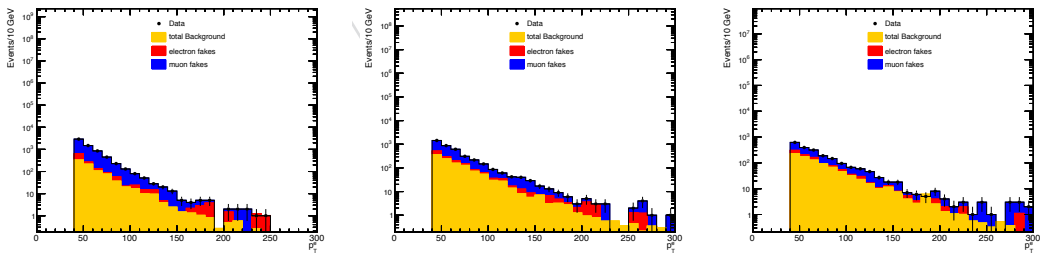


Figure 5: Misidentified lepton composition in data for 0-jet (left), 1-jet (mid) and 2-jet (right) after preselection in the isolation sideband, where one of the leptons is non-isolated. For prompt lepton contamination (yellow) is corrected using MC simulations.

301 The ratio f_μ of isolated to non-isolated muons is measured in an independent $Z \rightarrow \mu\mu$ dataset.
 302 $Z \rightarrow \mu\mu$ events are selected and additional muons are used as probe objects. The prompt
 303 lepton contamination arising from di-boson processes ($W\gamma^{(*)}$, WW, WZ, ZZ) is estimated using
 304 MC simulation and the ratio is corrected accordingly. In Figure 6 the ratio is shown.

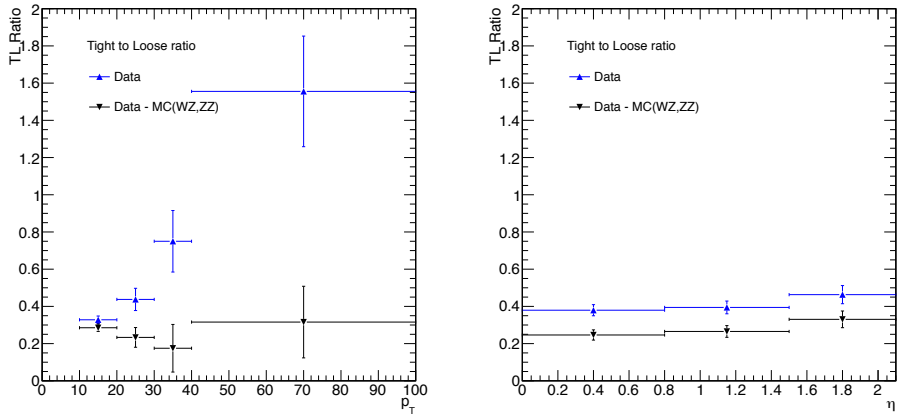


Figure 6: Measured isolated to non-isolated muon ratio (f_μ) as a function of the muon transverse momentum (left) and pseudorapidity (right).

The region with an isolated electron and a non-isolated muon is used to estimate the misidentified lepton background. First the prompt lepton backgrounds in this region are subtracted. The ratio of isolated to non-isolated muons is defined as

$$f_\mu = \frac{N[\mu(\text{isolated})]}{N[\mu(\text{not - isolated})]}. \quad (6)$$

Hence the background is given by:

$$N_\mu[\mu(\text{isolated})] = f_\mu N[\mu(\text{not - isolated})]. \quad (7)$$

305 The data-driven estimate of misidentified muons is validated using a same-sign $e\mu$ region.
 306 Figure 7 shows a comparison of measured and expected kinematic distributions in the region
 307 with like-sign leptons. Generally a good agreement between predictions and data is observed.

308 6.1.2 $Z \rightarrow \tau\tau$

309 The significant source of background in the $H \rightarrow e\tau_\mu$ channel is $Z \rightarrow \tau\tau$ decays in which one τ
 310 decays to an electron plus neutrinos and the other to a muon and a neutrino. This background
 311 is estimated using the particle flow embedding technique [25]. A sample of $Z \rightarrow \mu\mu$ events is
 312 taken from data using a loose selection. The muons are then replaced with simulated τ decays
 313 reconstructed with the particle flow algorithm. Thus the key features of the event topology
 314 such as the jets, missing energy and underlying event are taken directly from data with only
 315 the τ decays being simulated. The normalization of the sample is from the Monte Carlo ex-
 316 pectation. A comparison of the collinear mass distribution from $Z \rightarrow \tau\tau$ MC and embedding
 317 technique is shown in Figure 8. A shift of 2% of the embedded sample with respect to MC
 318 simulation is observed. This shift corrects a bias in the embedding technique, which does not
 319 take FSR photons into account. Identification and isolation corrections derived by comparing
 320 MC simulations and the particle flow embedded samples are shown in Figure 9.

321 6.1.3 $t\bar{t} \rightarrow l\nu l\nu b\bar{b}$

322 The $t\bar{t}$ process, where both top quarks are decaying via a W boson into an electron, muon and
 323 additional neutrinos is an important background, especially in the 1-jet and 2-jet event cate-
 324 gories. Vetoing events with any number of b-tagged jets suppresses this background signifi-
 325 cantly. MC simulations are used to estimate the remaining contributions. The normalization

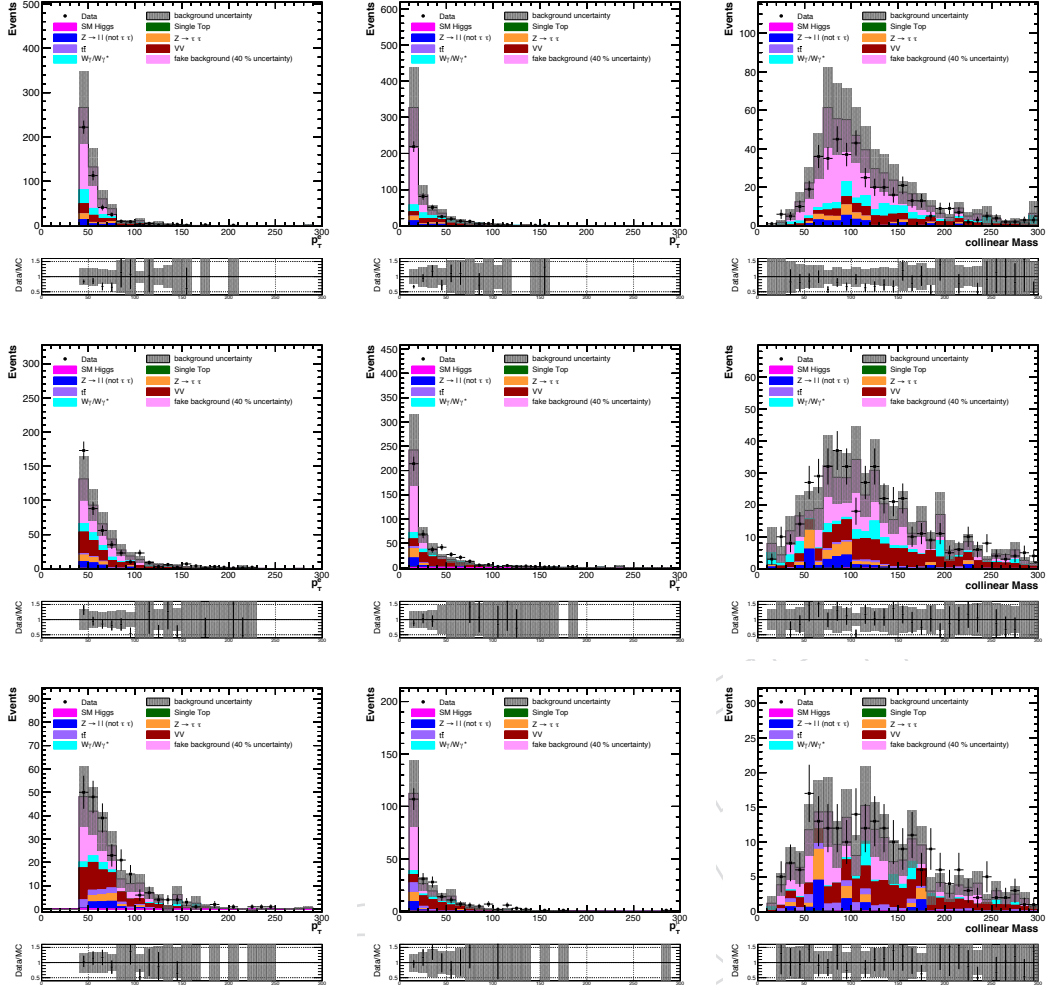


Figure 7: Measured and simulated kinematic distributions after preselections in the same-sign control region for the 0-jet (upper row), 1-jet (mid row) and 2-jet (lower row) event categories. From left to right: electron p_T , muon p_T , and collinear mass.

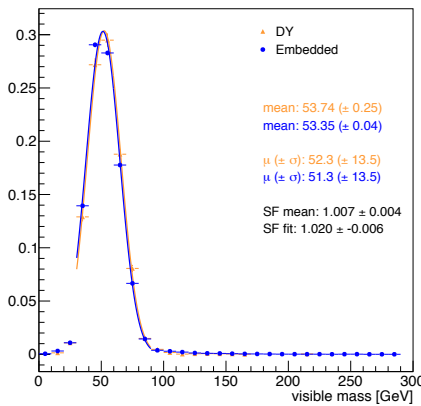


Figure 8: Collinear mass distribution for the $Z \rightarrow \tau\tau$ MC and embedding technique.

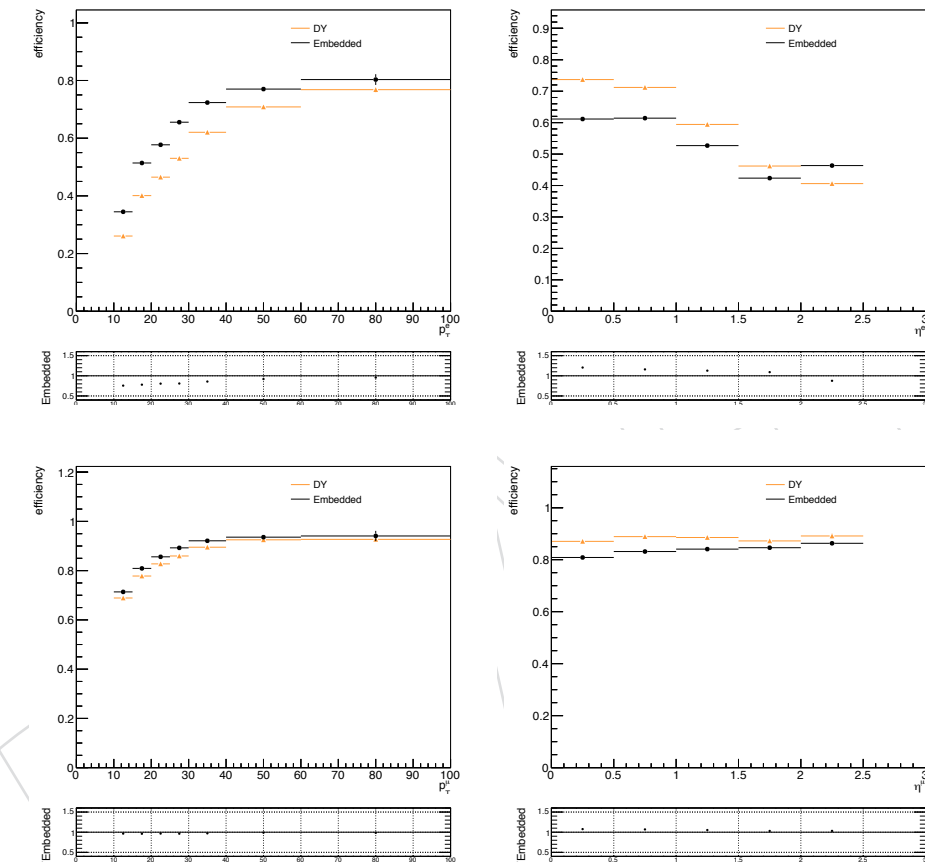


Figure 9: Electron (top row) and Muon (lower row) identification and isolation correction factors as a function of the electron transverse momentum (left) pseudorapidity(right) for the $Z \rightarrow \tau\tau$ pf embedded sample .

of the $t\bar{t}$ process is cross checked in a $t\bar{t}$ enriched control sample. The latter is defined by pre-selection cuts for the 2-jet category, but requiring at least one b-tagged jet. In Figure 10 the comparison of predictions and data is shown. Good agreement is observed.

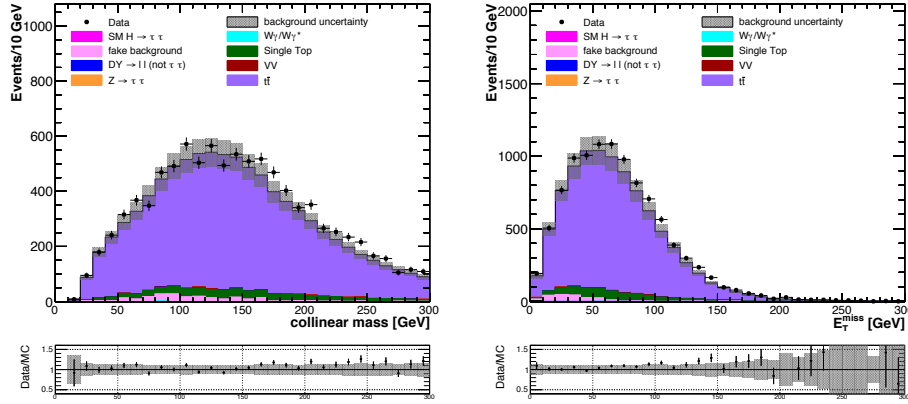


Figure 10: Collinear mass (left) and E_T^{miss} (right) distributions in the $t\bar{t}$ control region.

6.1.4 Other backgrounds

Other smaller backgrounds come from WW , $ZZ + jets$, $W\gamma + jets$ and single top production. SM Higgs decays in the $H \rightarrow \tau\tau$ channel are also taken into account. This background is suppressed by the kinematic selection criteria. Each of these is estimated with simulation.

6.2 Background estimates for $H \rightarrow e\tau_{had}$

6.2.1 W+jets and other sources of misidentified taus and electrons

The $W + jets$ process is an important background to LFV Higgs signal in the $H \rightarrow e\tau_{had}$ channel when the W decays to an electron and neutrino and the jet is misidentified as hadronic τ decay. Other minor sources of jet faking a τ are QCD jet events, $Z(ee) + jets$ in which one of the electrons is undetected or escapes the veto and a jet is misidentified as the hadronic τ decay. Furthermore, in $t\bar{t}$ events a W can decay to electron and neutrino while the other W decays either hadronically or to a lepton which is either undetected or escapes the veto, and one of the jets is misidentified as the hadronic τ . These minor backgrounds will also be accounted for in this method.

The misidentification rate f_τ is measured from the ratio of $Z(ee) + X$ event candidates, where X is a τ candidate reconstructed with different working points

$$f_\tau = \frac{N[Z(ee) + \tau(\text{tight})]}{N[Z(ee) + \tau(\text{loose})]} \quad (8)$$

where *tight* and *loose* refer to the τ isolation requirement and correspond to `tightIsoHits3` and `looseIsoHits3`, respectively. The $Z(ee)$ candidates are selected by imposing the following requirements:

- All electron candidates

- $p_T > 30 \text{ GeV}$
- $|\eta| < 1.4442$ or $1.566 < |\eta| < 2.3$
- no Missing Hits, conversions veto

- 350 • ChargeIdLoose
 351 • JetCSVBtag < 0.8
 352 • JetBtag < 3.3
 353 • dz < 0.2 cm
 354 • MuonIdIsoVtxOverlap=True
 355 • **Z candidate electrons**
 356 • MVA ID “tight”
 357 • RelPFIsoDB < 0.10

Figure 11 shows the measured misidentification rate compared with simulated Z+jets events.

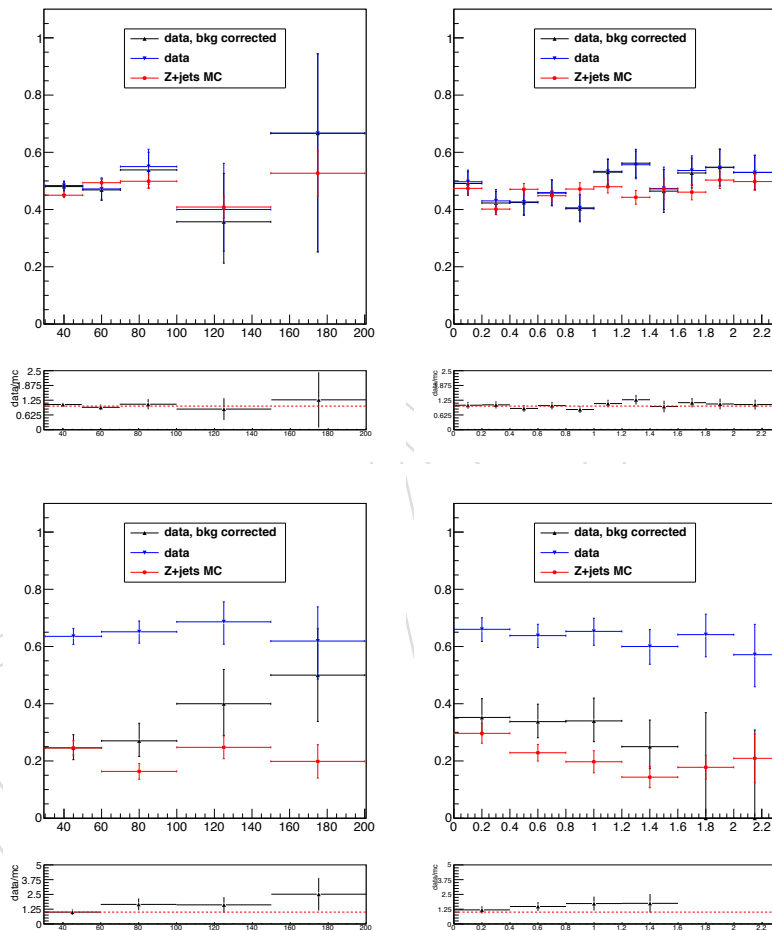


Figure 11: Measured and simulated τ (upper row) and electron (lower row) misidentification rate as a function of the lepton p_T (left) and pseudorapidity (right).

358

The region with an isolated electron and a not-tightly-isolated τ is used to estimate the W + jets background. First, the backgrounds in this region are subtracted. The ratio of isolated to non-isolated τ candidates is given by

$$\frac{N[\tau(\text{tight})]}{N[\tau(\text{loose \& not - tight})]} = \frac{f_\tau}{1 - f_\tau} \frac{N[\tau(\text{loose})]}{N[\tau(\text{loose})]}. \quad (9)$$

Hence the background is given by:

$$N_\tau[\tau(\text{tight})] = \frac{f_\tau}{1-f_\tau} N[\tau(\text{loose \& not - tight})]. \quad (10)$$

As a cross-check, the τ misidentification rate is also determined in a QCD-enriched region selected applying the same selection applied for the $Z(ee) + X$ region with the exception of the following requirements: “loose” and anti-isolated MVA electron with $p_T > 15$ GeV and $\text{RelPFIsoDB} > 0.2$. The averaged values of f_τ extracted in this region are reported in Table 8 and shown in Fig. 12 as a function of τp_T . The measured fake rates are well within the 30% systematic uncertainty assigned.

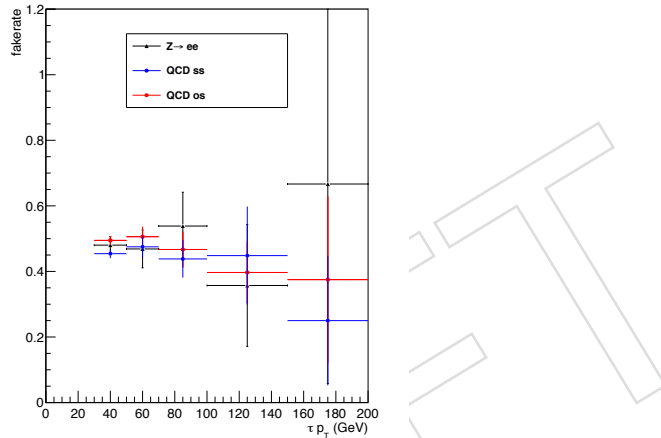


Figure 12: Measured τ misidentification rate as a function of the lepton p_T in different kinematic regions (see text).

Table 8: Average τ misidentification rates, f_τ , measured in different kinematic regions, where OS (SS) represent opposite charge (same charge) leptons.

Region	f_τ
$Z \rightarrow e^+e^-$	0.490 ± 0.012
QCD OS	0.494 ± 0.007
QCD SS	0.455 ± 0.008

A similar procedure is adopted to measure the electron misidentification rate, with the corresponding factor, f_e , defined as:

$$f_e = \frac{N[Z(ee) + e(\text{tight})]}{N[Z(ee) + e(\text{loose})]} \quad (11)$$

where the loose and tight working points of the MVA electron identification are used with $\text{RelPFIsoDB} < 0.20$ and 0.1, respectively. The measured and simulated electron misidentification rates are shown in Figure 11. While the τ misidentification rates are found to be well described by MC simulation, the electron misidentification are substantially underestimated

in the simulation. To avoid double counting, the total amount of misidentified objects is computed from

$$N_{tot}^{fakes} = N_\tau + N_{elec} - \frac{f_e}{1-f_e} \frac{f_\tau}{1-f_\tau} N[\tau(\text{loose \& not tight}) \wedge \text{electron(loose \& not tight)}]. \quad (12)$$

The data-driven estimate of electron and τ leptons is validated using a same-sign $e\tau_{had}$ region. Figure 13 shows a comparison of measured and expected kinematic distributions in the region with like-sign leptons. Good agreement is observed in all kinematic distributions.

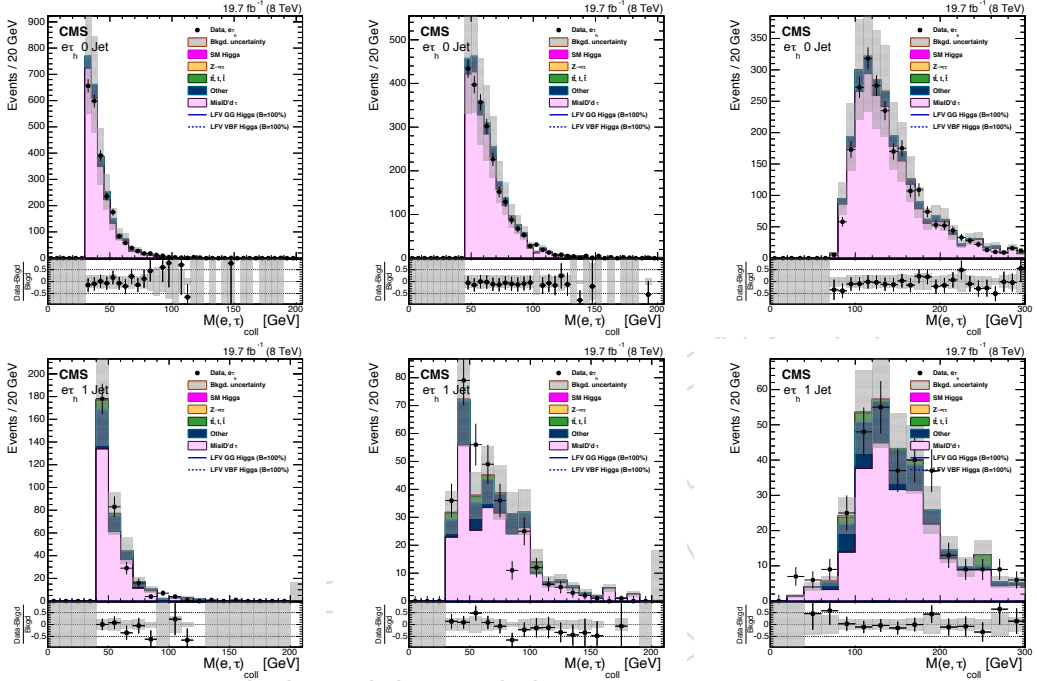


Figure 13: Measured and simulated kinematic distributions after all the selections in the same-sign control region for the 0-jet (upper row) and 1-jet (lower row) event categories. From left to right: τp_T , electron p_T , and collinear mass.

367

6.2.2 $Z \rightarrow \tau\tau$

Another significant source of background in the $H \rightarrow e\tau_{had}$ channel are $Z \rightarrow \tau\tau$ decays in which one τ decays to a electron plus neutrinos and the other hadronically. This background is estimated using the particle flow embedding technique [25]. A sample of $Z \rightarrow \mu\mu$ events is taken from data using a loose selection. The muons are then replaced with simulated τ decays reconstructed with the particle flow algorithm. Thus the key features of the event topology such as the jets, missing energy and underlying event are taken directly from data with only the τ decays being simulated. The normalization of the sample is from the Monte Carlo expectation. A comparison of the collinear mass distribution from $Z \rightarrow \tau\tau$ MC and embedding technique is shown in Figure 14. The peak position agrees within the fit uncertainties and no further correction is applied.

As a further cross check, Figure 15 shows a comparison of data to expectations for a control region characterized by an enhanced $Z \rightarrow \tau\tau$ contribution. This region is defined by the baseline preselection of the 2-jet category with $\Delta R_{e-\tau} < 2$. The choice of the 2-jet category is due

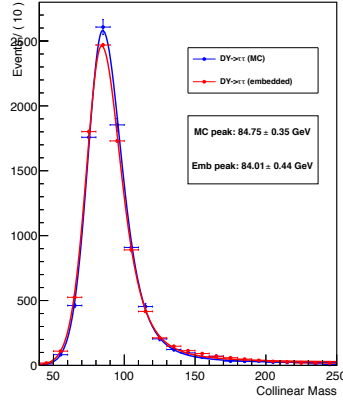


Figure 14: Collinear mass distribution for the $Z \rightarrow \tau\tau$ MC and embedding technique.

382 to the shape of the ΔR distributions, which allows a more effective separation of $Z \rightarrow \tau\tau$ can-
 383 didates from the misidentified τ background. Good agreement is observed between measured
 and expected backgrounds.

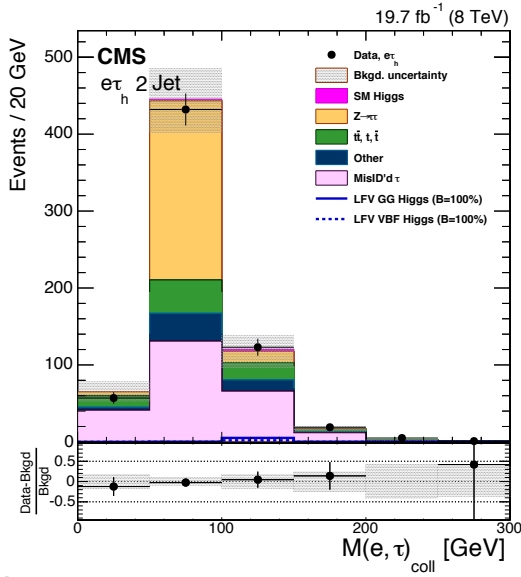


Figure 15: Collinear mass for the control region enriched in $Z \rightarrow \tau\tau$ background in the $e\tau_{had}$ 2-jet channel.

384

385 6.2.3 Other backgrounds

386 The other sources of background are all estimated from Monte Carlo both for the distribution
 387 shape and normalization. These backgrounds are $Z+jets$ with an electron being misidentified
 388 as τ , $t\bar{t}+jets$, $WW+jets$ and single top events.

389 6.2.4 Standard Model Higgs backgrounds

390 The standard model Higgs Boson provides a background to LFV Higgs decays. The most
 391 significant is the $H \rightarrow \tau\tau$ process. Table 9 gives the expected event yields for the $H \rightarrow e\tau_{had}$

³⁹² in the signal region $100 \text{ GeV} < M_{col} < 150 \text{ GeV}$ from the four production processes gluon
³⁹³ fusion, vector boson fusion, associated vector boson, and associated top quark production.
³⁹⁴ Also considered are the decays $H \rightarrow WW$. The yields from LFV Higgs with $B(H \rightarrow \mu\tau) = 1\%$
³⁹⁵ are also given for reference.

$H \rightarrow e\tau$ (Gluon Fusion)	87.42 ± 6.13	20.02 ± 1.80	1.96 ± 0.53
$H \rightarrow e\tau$ (Vector Boson Fusion)	0.54 ± 0.03	1.59 ± 0.08	2.11 ± 0.30
$H \rightarrow \tau\tau$ (Gluon Fusion)	12.66 ± 0.99	3.07 ± 0.31	0.41 ± 0.11
$H \rightarrow \tau\tau$ (Vector Boson Fusion)	0.18 ± 0.05	0.46 ± 0.04	0.92 ± 0.16
$WH(\tau\tau) + ZH(\tau\tau) + t\bar{t}H(\tau\tau)$	0.25 ± 0.01	0.27 ± 0.01	-
$H \rightarrow WW$ (Gluon Fusion)	-	-	-
$H \rightarrow WW$ (Vector Boson Fusion)	-	-	-
$WH(WW) + ZH(WW) + t\bar{t}H(WW)$	0.04 ± 0.01	-	-
$H \rightarrow bb$ (Gluon Fusion)	-	-	-
$H \rightarrow bb$ (Vector Boson Fusion)	0.04 ± 0.01	0.02 ± 0.01	0.03 ± 0.01

Table 9: Event yields in the signal region $100 \text{ GeV} < M_{collinear} < 150 \text{ GeV}$ for the LFV Higgs with $B(H \rightarrow e\tau)=1\%$ and the Standard Model Higgs backgrounds. The expected contributions are normalized to an integrated luminosity of 19.7 fb^{-1}

396 7 Comparison of measured and expected distributions

397 7.1 $e\tau_\mu$ channel

398 The expected signal, background distributions using MC, and data-driven background esti-
 399 mations described in section 6.1 are shown in Figures 16, 17 and 18 for the $e\tau_\mu$ channel in the
 400 0-jet, 1-jet and 2-jet categories, respectively.

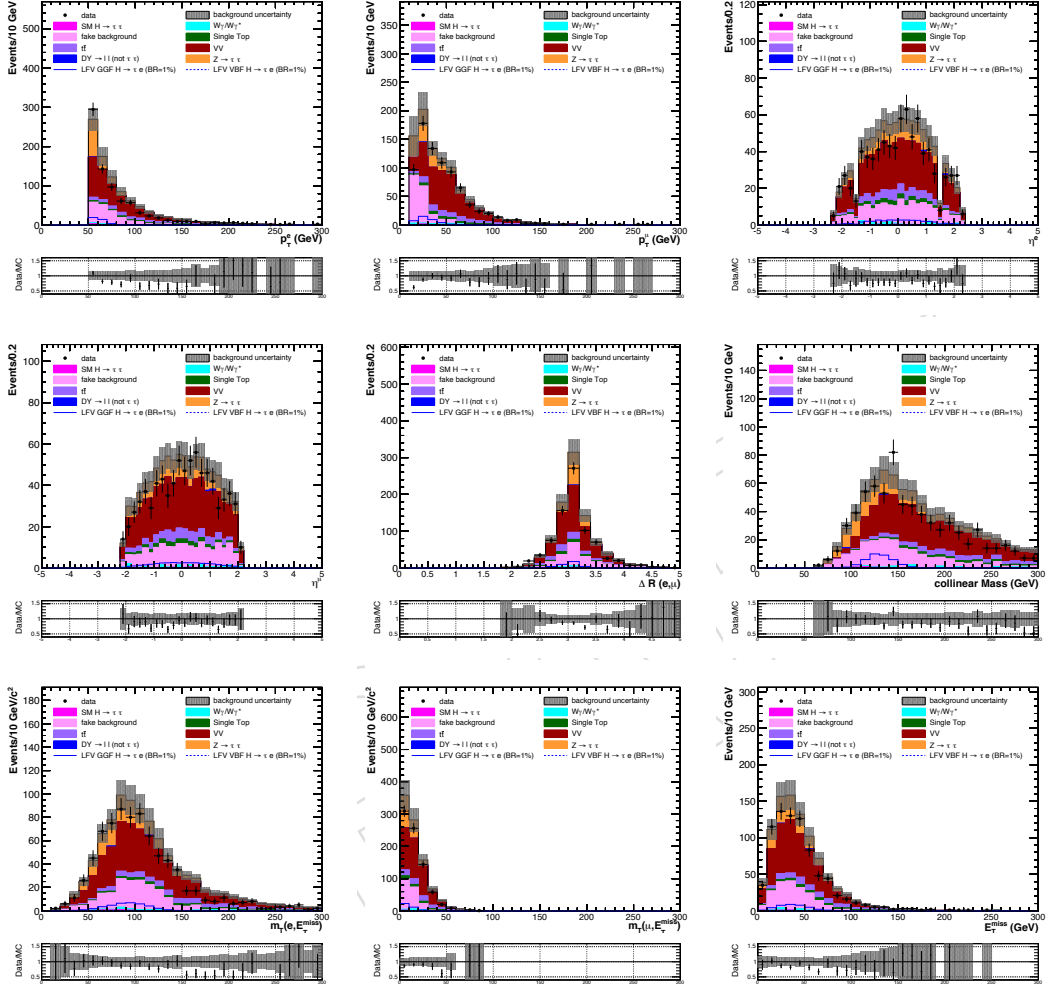


Figure 16: Measured and expected (pre-fit) kinematic distributions of the $e\tau_\mu$ channel after all selection cuts for the 0-jet category. From left to right and top to bottom: electron p_T , muon p_T , electron pseudorapidity, muon pseudorapidity, $\Delta R(e, \mu)$, collinear mass, transverse mass of electron and PFMET, transverse mass of muon and PFMET, and PFMET.

401 7.2 $e\tau_{had}$ channel

402 The expected signal and background using MC and data-driven background estimates com-
 403 pared to data, after all the selection requirements, are shown in Figures 19, 20, and 21 for the
 404 $e\tau_{had}$ channel in the 0-jet, 1-jet and 2-jet categories, respectively. The shaded areas represent
 405 the quadratic sum of the systematic uncertainties on the background expectations discussed in
 406 Section 8.

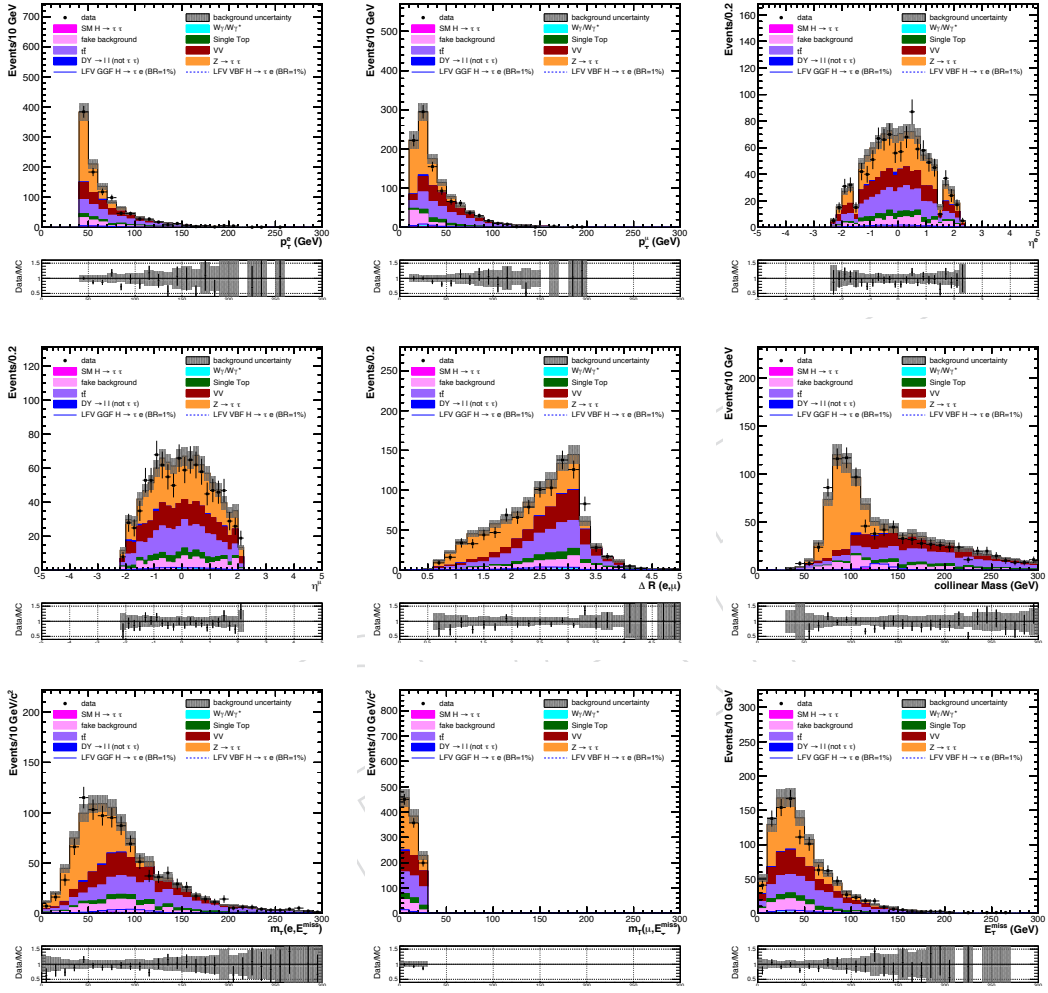


Figure 17: Measured and expected (pre-fit) kinematic distributions of the $e\tau_\mu$ channel after all selection cuts for the 1-jet category. From left to right and top to bottom: electron p_T , muon p_T , electron pseudorapidity, muon pseudorapidity, $\Delta R(e, \mu)$, collinear mass, transverse mass of electron and PFMET, transverse mass of muon and PFMET, and PFMET

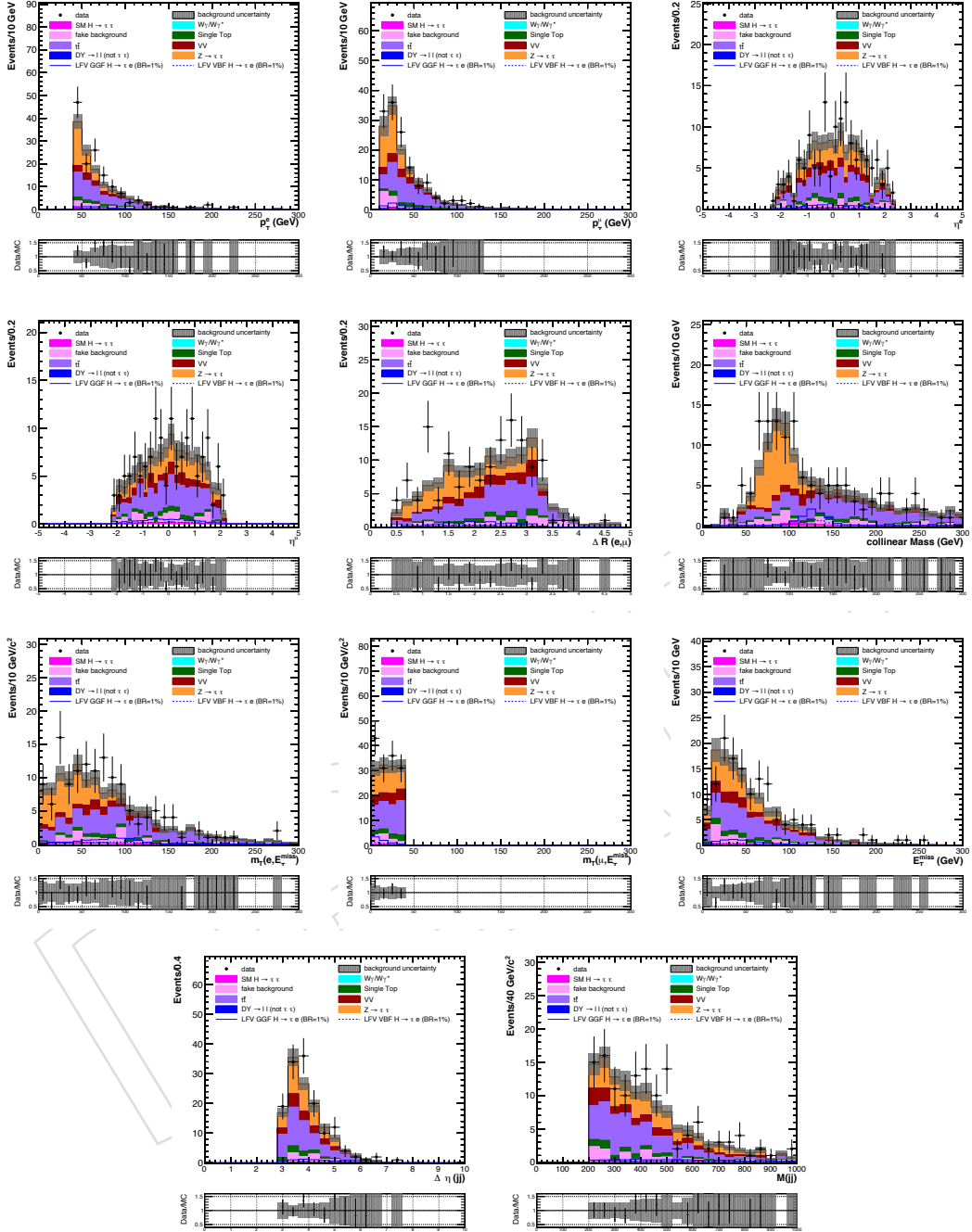


Figure 18: Measured and expected (pre-fit) kinematic distributions of the $e\tau_\mu$ channel after all selection cuts for the 2-jet category. From left to right and top to bottom: electron p_T , muon p_T , electron pseudorapidity, muon pseudorapidity, $\Delta R(e, \mu)$, collinear mass, transverse mass of electron and PFMET, transverse mass of muon and PFMET, PFMET, difference in pseudorapidity of the two jets, and the dijet mass.

7 Comparison of measured and expected distributions

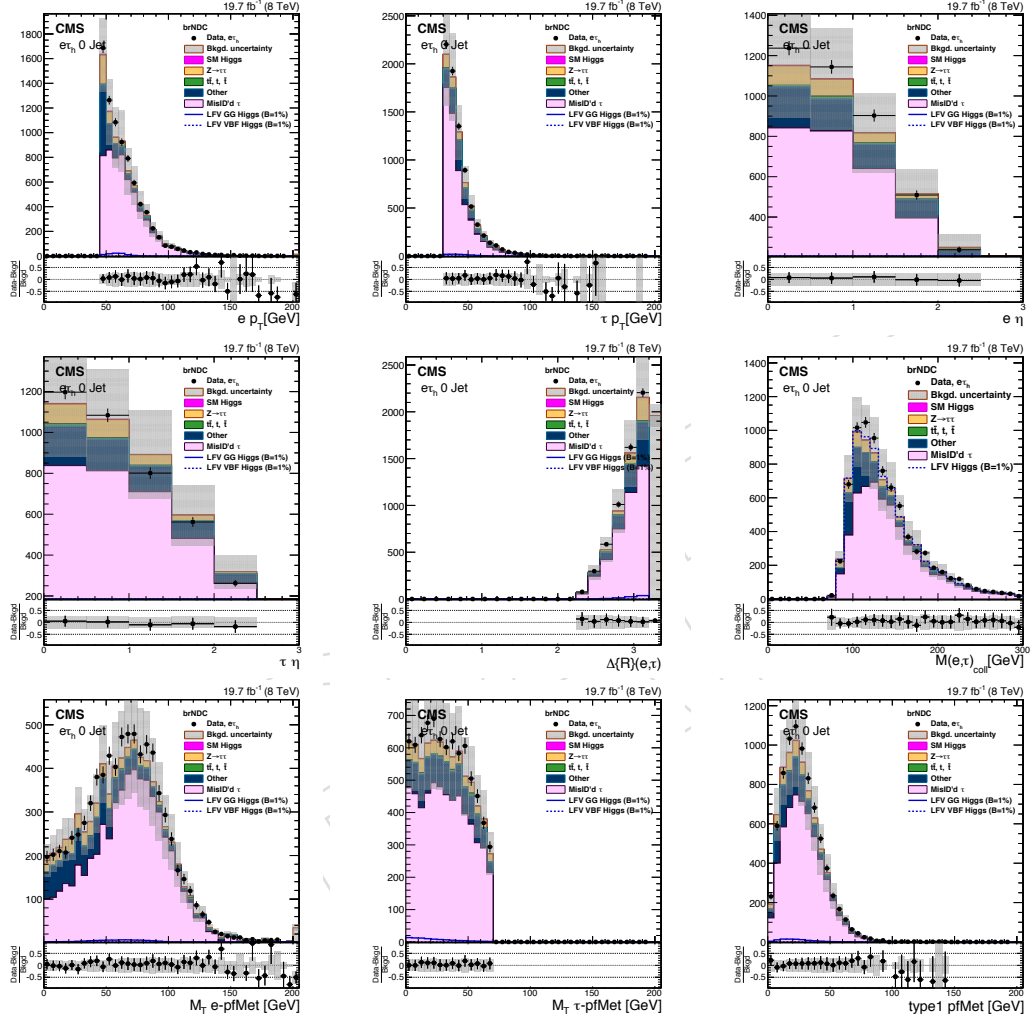


Figure 19: Measured and expected (pre-fit) kinematic distributions of the $e\tau_{had}$ channel after all selection cuts for the 0-jet category. From left to right and top to bottom: electron p_T , τp_T , electron pseudorapidity, τ pseudorapidity, $\Delta R(e, \tau)$, collinear mass, transverse mass of electron and PFMET, transverse mass of τ and PFMET.

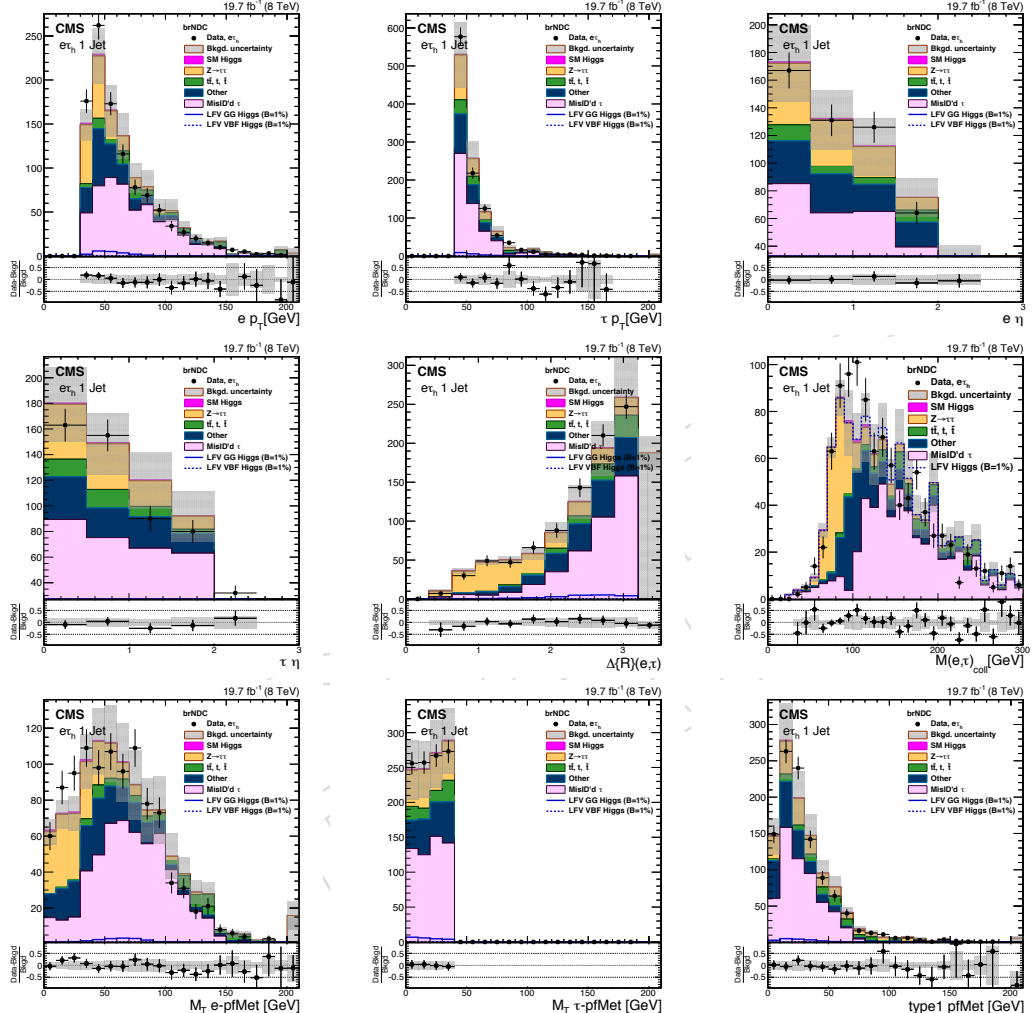


Figure 20: Measured and expected (pre-fit) kinematic distributions of the $e\tau_{had}$ channel after all selection cuts for the 1-jet category. From left to right and top to bottom: electron p_T , τ p_T , electron pseudorapidity, τ pseudorapidity, $\Delta R(e, \tau)$, collinear mass, transverse mass of electron and PFMET, transverse mass of τ and PFMET.

7 Comparison of measured and expected distributions

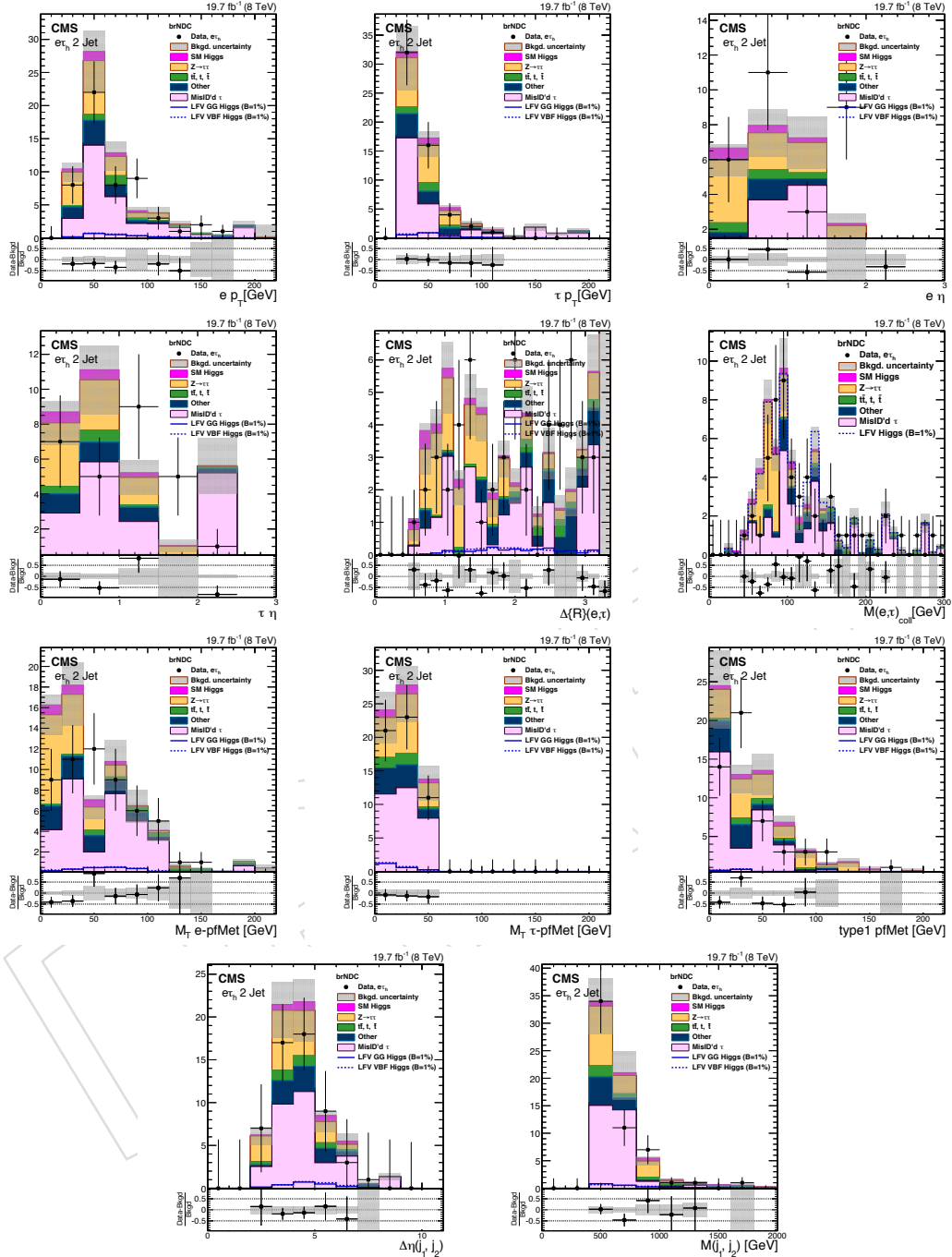


Figure 21: Measured and expected (pre-fit) kinematic distributions of the $e\tau_{had}$ channel after all selection cuts for the 2-jet category. From left to right and top to bottom: electron p_T , τp_T , electron pseudorapidity, τ pseudorapidity, $\Delta R(e, \tau)$, collinear mass, transverse mass of electron and PFMET, transverse mass of τ and PFMET, PFMET, difference in pseudorapidity of the two jets, and the dijet mass

407 8 Systematic errors

408 The presence or absence of a signal is established using the asymptotic CL_s method as recom-
 409 mended by the Higgs combination group. Shape templates of M_{col} distributions for the various
 410 background sources are used. The expected signal and background is then binned in M_{col} and
 411 a likelihood technique is used to estimate the signal strength μ which in turn can be used to
 412 set confidence limits in the absence of a signal. The systematics that do not affect the final M_{col}
 413 shapes of the templates are treated as yield-only *nuisances*, while for the others we also take
 414 into account the difference in shape by providing one-sigma-shifted templates and allowing
 415 the fit to interpolate between them and the central value.

416 8.1 Nuisance parameters

Table 10: Nuisance parameters for the $e\tau_{had}$ channel

Systematic	H $\rightarrow e\tau_{had}$		
	0-jet	1-jet	2-jet
Electron Trigger/ID/Isolation	1%	1%	2%
Hadronic tau efficiency	6.7%	6.7%	6.7%
Luminosity	2.6%	2.6%	2.6%
$Z \rightarrow \tau\tau$ background	$3 \oplus 5\%$	$3 \oplus 5\%$	$3 \oplus 10\%$
$Z \rightarrow \mu\mu, ee$ background	30%	30%	30%
Reducible background normalization	30%	30%	30%
Diboson background	15%	15%	15%
top pair background	10%	10%	$10 \oplus 33\%$
single top background	10%	10%	10%
Higgs gluon fusion production	$9.7 \oplus 4 \oplus 8\%$		
Higgs VBF production	$3.6 \oplus 10 \oplus 4\%$		

Table 11: Nuisance parameters for the $e\tau_\mu$ channel

Systematic	H $\rightarrow e\tau_{mu}$		
	0-jet	1-jet	2-jet
Electron Trigger/ID/Isolation	3%	3%	3%
Muon Trigger/ID/Isolation	2%	2%	2%
Luminosity	2.6%	2.6%	2.6%
B-Tagging veto	3%	3%	3%
$Z \rightarrow \tau\tau$ background	$3 \oplus 5\%$	$3 \oplus 5\%$	$3 \oplus 10\%$
$Z \rightarrow \mu\mu, ee$ background	30%	30%	30%
Reducible background normalization	40%	40%	40%
Diboson background	15%	15%	15%
top pair background	10%	10%	$10 \oplus 10\%$
single top background	10%	10%	10%
Higgs gluon fusion production	$9.7 \oplus 4 \oplus 8\%$		
Higgs VBF production	$3.6 \oplus 10 \oplus 4\%$		

417 The systematic errors are summarized in Tables 10 and 11. The uncertainties associated to
 418 the predictions for Higgs production are reported in Table 12. The uncertainty in the electron
 419 and muon selection (trigger, identification and isolation) are estimated using the tag and probe

technique in $Z \rightarrow \mu\mu, ee$ data. The hadronic τ efficiency is estimated using tag and probe in $Z \rightarrow \tau\tau$ data [26, 27]. The $Z \rightarrow \tau\tau$ background is estimated by the embedding technique as described in sections 6.1.2 and 6.2.2 and the uncertainty in this is predominantly from the uncertainty in the τ efficiency. The uncertainties in the estimation of the misidentification rate are the recommended uncertainties from the τ POG. The remaining uncertainties are from the uncertainty in the cross-section of the backgrounds that have been estimated by Monte Carlo.

There are several uncertainties that arise from the theoretical uncertainty in the H production cross section, which differ for each production mechanism contribution within each category. They are given in Table 12 and the numbers used are the same as for the SM $H \rightarrow \tau\tau$ analysis. These affect the LFV Higgs and the SM Higgs background equally, and are treated as 100% correlated. The parton distribution function (PDF) uncertainty is evaluated by comparing the yields in each category, when spanning the parameter range of a number of different independent PDF sets including CT10 [28], MSTW [29], NNPDF [30] as recommended by PDF4LHC [31]. The scale uncertainty is estimated by varying the renormalization, μ_R , and factorization scale, μ_F , up and down by one half or two times the nominal scale ($\mu_R = \mu_F = M_H/2$) under the constraint $0.5 < \mu_R/\mu_F < 2$. The underlying event and parton shower uncertainty is estimated by using two different PYTHIA tunes, AUET2 and Z2*. Anticorrelations arise due to migration of events between the categories and are expressed as negative numbers.

Table 12: Theoretical uncertainties in Higgs production

Uncertainty	Gluon Fusion			Vector Boson Fusion		
	0-jet	1-jet	2-jet	0-jet	1-jet	2-jet
Parton Density Function	+9.7%	+9.7%	+9.7%	+3.6%	+3.6%	+3.6%
Renormalization Scale	+8 %	+10 %	-30%	+4 %	+1.5%	+2%
Underlying Event/Parton Shower	+4%	-5%	-10%	+10%	<1%	-1%

437

438 8.2 Systematic uncertainties in the template shapes

439 The systematic uncertainties in the shapes of the signal and background templates (i.e. the systematic uncertainties that depend on M_{col}) are summarized in table 13.

Table 13: Systematic uncertainties in the shape of the signal and background templates

Systematic	$H \rightarrow e\tau_\mu$	$H \rightarrow e\tau_{had}$
Hadronic τ energy scale	-	3%
Jet Energy scale	3-7%	3-7%
Unclustered energy scale	10%	10 %
$Z \rightarrow \tau\tau$ Bias	$2 \pm 2\%$	-
$Z \rightarrow ee$ Bias	-	5%

440

441 For the embedded $Z \rightarrow \tau\tau$ M_{col} distribution a 2% shift has been observed with respect to
 442 $Z \rightarrow \tau\tau$ Monte Carlo simulations by comparing the means of both templates [25]. This occurs
 443 only in the $H \rightarrow e\tau_\mu$ channel. The template has been corrected for this effect and a 100%
 444 uncertainty on this shift is used.

445 For the $Z \rightarrow ee$ in the hadronic channel a systematics of 5% has been considered to account the
 446 mismeasured energy of the electron reconstructed as a τ . This uncertainty has been extracted

447 from a control region obtained inverting the anti-electron discriminator requirement in the τ
 448 identification. This control region is dominated by $Z \rightarrow ee$ event. The parameters obtained
 449 from a fit to the data are used to fit the M_{col} distribution from the Monte Carlo sample adding a
 450 scale factor in the fitting function (Figure 22). This scale factor is the only free parameter of the
 451 fit. It is expected to be 1 if the simulated sample well represents the data. The uncertainty of
 452 the fitted scale factor is thus used as systematics uncertainty to allow variations of the $Z \rightarrow ee$
 shape.

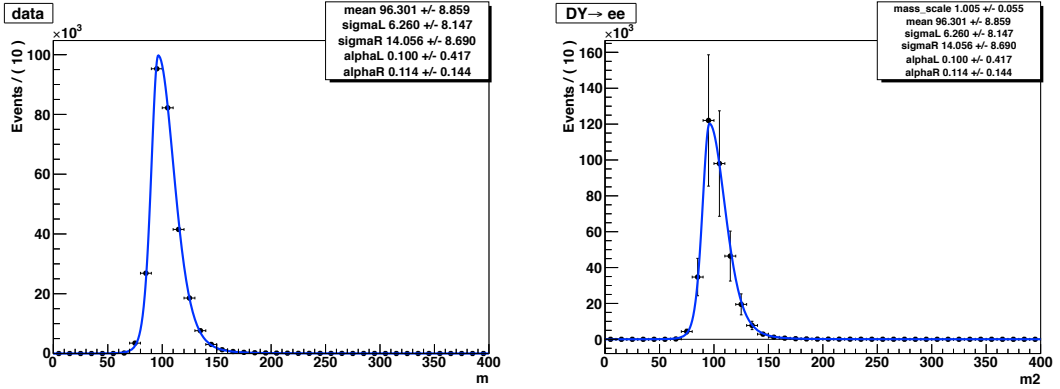


Figure 22: Fitted $Z \rightarrow ee M_{col}$ in data (left) and Monte Carlo (right) from the inverted anti-electron discriminator control region

453

454 The jet energy scale has been studied extensively by the CMS collaboration and a standard
 455 prescription is used in all analysis [32]. The uncertainties are applied as a function of η and
 456 η including all correlations. The overall scale is set using photon+jets events and the most
 457 significant uncertainty is in the photon energy scale. A number of other uncertainties such as
 458 jet fragmentation modelling, single pion response and uncertainties in the pileup corrections
 459 are also included. The jet energy scale uncertainties are propagated to the missing energy.
 460 There is also an additional uncertainty added to account for the unclustered energy scale un-
 461 certainty. The unclustered energy comes from jets below 10 GeV and particle flow candidates
 462 not within jets. It also is propagated to the missing energy. The τ energy scale is estimated
 463 by comparing $Z \rightarrow \tau\tau$ events in data and Monte Carlo. Good agreement is found and a 3%
 464 uncertainty is assigned. Finally the shape templates have a bin-by-bin statistical uncertainty
 465 that is also included.
 466 Potential uncertainties in the shape of the misidentified lepton backgrounds have also been
 467 considered. The procedure for estimating the misidentified lepton contributions is described
 468 in sections 6.2.1 and 6.1.1. In the $H \rightarrow e\tau_{had}$ channel the misidentification rates are applied as a
 469 function of η . The uncertainty of the misidentification rate function is propagated to obtain the
 470 different shapes to be used as systematics in the fit. In the $H \rightarrow e\tau_\mu$ channel the misidentifica-
 471 tion rates are applied in bins of p_T and η . These rates are adjusted all up or down by 1 σ . The
 472 different shapes are then used as systematics in the fit.

473 9 Results

474 The unblinded pre-fit and post-fit M_{col} distributions are shown in Figures 23 and 24.
 475 The pre-fit event yields in the mass ranges $50 \text{ GeV} < M_{col} < 300 \text{ GeV}$ and $100 \text{ GeV} < M_{col} <$
 476 150 GeV are shown in Tables 14 and 15 for the $e\tau_{had}$ channel, respectively. The corresponding

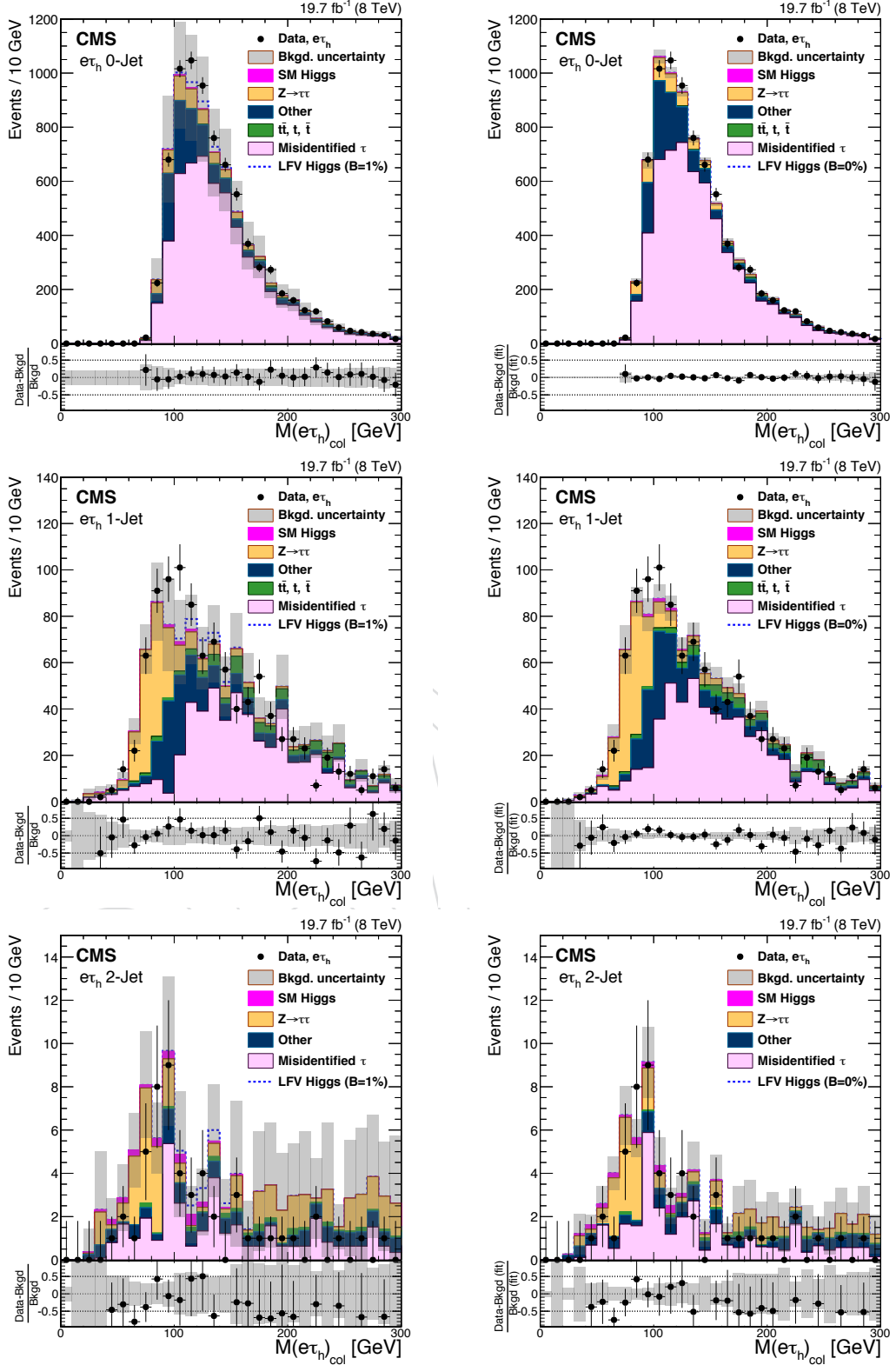


Figure 23: Pre-Fit (left) and postfit (right) for the 0 jet (top), 1 jet (middle), 2 jet (bottom) category for the $H \rightarrow e\tau_{had}$ channel

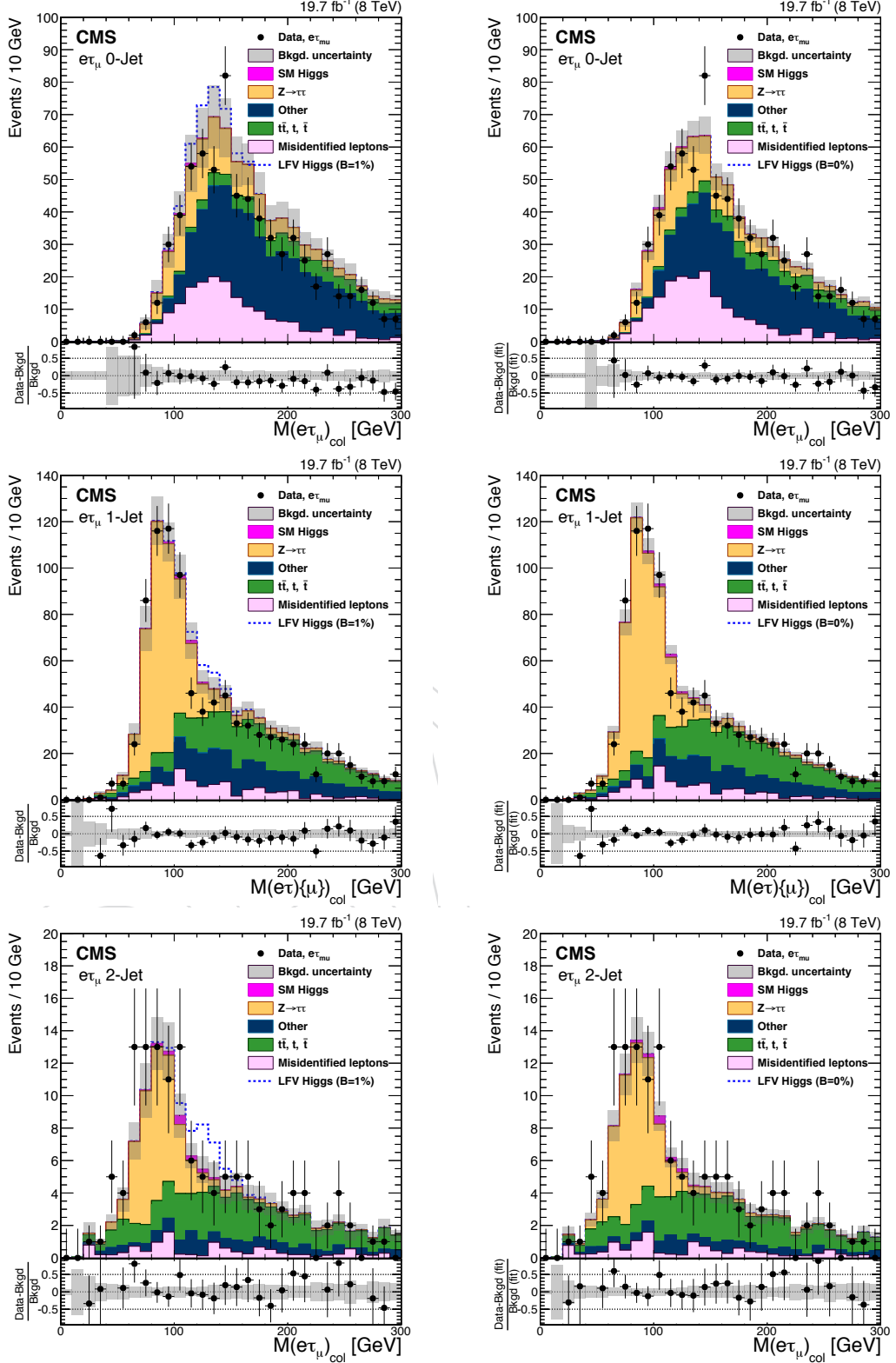


Figure 24: Pre-Fit (left) and postfit (right) for the 0 jet (top), 1 jet (middle), 2 jet (bottom) category for the $H \rightarrow e\tau_\mu$ channel

jet category :	0-Jet	1-Jet	2-Jet
Fakes	5609.74 ± 438.91	510.41 ± 43.70	33.89 ± 7.79
$Z \rightarrow ee, \mu\mu$	988.37 ± 227.66	166.20 ± 30.76	13.79 ± 2.10
$Z \rightarrow \tau\tau$	529.91 ± 16.70	212.51 ± 12.42	36.20 ± 9.30
$t\bar{t}$	20.37 ± 1.26	27.87 ± 1.59	3.44 ± 0.70
t, \bar{t}	32.99 ± 7.46	47.81 ± 9.20	-
EWK Diboson	173.33 ± 6.70	27.10 ± 1.11	1.78 ± 0.18
SM Higgs Background, ggf	15.81 ± 1.06	5.07 ± 0.41	0.62 ± 0.13
SM Higgs Background, vbf	0.23 ± 0.06	0.84 ± 0.09	2.18 ± 0.28
Sum of Background	7370.76 ± 487.90	997.80 ± 55.21	91.90 ± 12.48
LFV Higgs Signal	94.52 ± 6.17	22.76 ± 1.84	4.32 ± 0.72

Table 14: Event yield in the extended mass window $50 \text{ GeV} < M_{\text{collinear}} < 300 \text{ GeV}$ for the $H \rightarrow e\tau_{\text{had}}$ channel. Both systematics and statistics uncertainties are considered. The expected (pre-fit) contributions are normalized to an integrated luminosity of 19.7 fb^{-1} . The LFV Higgs signal is the MC expectation for $\text{B}(H \rightarrow e\tau) = 1\%$.

jet category :	0-Jet	1-Jet	2-Jet
Fakes	3136.44 ± 378.90	186.11 ± 28.02	9.60 ± 4.33
$Z \rightarrow ee, \mu\mu$	639.75 ± 142.02	77.96 ± 18.95	3.46 ± 1.26
$Z \rightarrow \tau\tau$	287.49 ± 12.97	32.97 ± 2.87	1.99 ± 0.62
$t\bar{t}(t)$	5.53 ± 0.63	6.73 ± 0.81	0.74 ± 0.33
$t, (\bar{t})$	5.19 ± 2.73	7.77 ± 3.79	-
EWK Diboson	69.08 ± 4.98	8.28 ± 0.67	0.43 ± 0.14
SM Higgs Background, ggf	12.66 ± 0.99	3.07 ± 0.31	0.41 ± 0.11
SM Higgs Background, vbf	0.18 ± 0.05	0.46 ± 0.04	0.92 ± 0.16
Sum of Background	4156.33 ± 396.88	323.34 ± 33.63	17.54 ± 4.56
LFV Higgs Signal	87.96 ± 6.15	21.61 ± 1.84	4.07 ± 0.72

Table 15: Event yield in the mass window $100 \text{ GeV} < M_{\text{collinear}} < 150 \text{ GeV}$ for the $H \rightarrow e\tau_{\text{had}}$ channel. Both systematic and statistic uncertainties are considered. The expected (pre-fit) contributions are normalized to an integrated luminosity of 19.7 fb^{-1} . The LFV Higgs signal is the MC expectation for $\text{B}(H \rightarrow e\tau) = 1\%$.

event yields for the $e\tau_\mu$ channel are shown in Tables 16 and 17. The different channels and categories are used to set a 95% CL upper limit on the branching fraction of lepton flavor violating higgs decay in $e\tau$ channel, $\text{BR}(H \rightarrow e\tau)$ as described in the previous section. The mean expected and observed 95% CL upper limits for Higgs boson mass at 125 GeV are summarized in Tables 18 and 19, respectively. Combining all the channels an expected upper limit of $0.75\% \pm 0.39\%$ for $H \rightarrow e\tau$ is obtained, while the observed upper limit is 0.69% . The best fit values for the branching fractions are given in table 20. No large deviations from zero have been observed. The event yields obtained from the fit are reported in Tables 21 and 22 for the $e\tau_{\text{had}}$ channel and Tables 23 and 24 for the $e\tau_\mu$ channel. The limits and best fit branching fractions are also summarized graphically for comparison in Figure 25.

jet category :	0-Jet	1-Jet	2-Jet
Fakes	163.93 ± 8.24	86.07 ± 6.08	9.87 ± 1.49
$Z \rightarrow ee, \mu\mu$	2.50 ± 0.81	7.24 ± 0.54	0.00 ± 0.00
$Z \rightarrow \tau\tau$	168.83 ± 3.01	415.07 ± 8.60	44.15 ± 1.86
$t\bar{t}$	56.63 ± 1.84	205.85 ± 4.14	37.18 ± 1.44
t, \bar{t}	24.39 ± 0.76	51.89 ± 1.34	6.49 ± 0.27
EWK Diboson	279.54 ± 4.97	149.82 ± 3.17	10.85 ± 0.67
$W\gamma$	1.75 ± 1.36	-	-
$W\gamma^*$	6.30 ± 1.88	1.18 ± 0.60	0.05 ± 0.03
SM Higgs Background, ggf	3.00 ± 0.36	4.39 ± 0.44	0.46 ± 0.15
SM Higgs Background, vbf	0.03 ± 0.01	0.46 ± 0.03	1.23 ± 0.07
Sum of Background	706.90 ± 9.30	921.96 ± 11.03	110.27 ± 2.86
LFV Higgs Signal	0.00 ± 0.09	0.00 ± 0.07	0.00 ± 0.03

Table 16: Event yield in the mass window $50 \text{ GeV} < M_{\text{collinear}} < 300 \text{ GeV}$ for the $H \rightarrow e\tau_\mu$ channel. Both systematics and statistics uncertainties are considered. The expected (pre-fit) contributions are normalized to an integrated luminosity of 19.7 fb^{-1} . The LFV Higgs signal is the MC expectation for $B(H \rightarrow e\tau) = 1\%$. “-” indicates that 0 MC events for the particular background are selected.

10 Exclusion limits on LFV Higgs Yukawa couplings

The LFV decays $H \rightarrow e\mu, e\tau, \mu\tau$ arise at tree level from the assumed flavor violating Yukawa interactions, Eq. 13 where the relevant terms are explicitly

$$L_V \equiv -Y_{e\mu}\bar{e}_L\mu_R h - Y_{\mu e}\bar{\mu}_L e_R h - Y_{e\tau}\bar{e}_L\tau_R h - Y_{\tau e}\bar{\tau}_L e_R h - Y_{\mu\tau}\bar{\mu}_L\tau_R h - Y_{\tau\mu}\bar{\tau}_L\mu_R h \quad (13)$$

The bounds on LFV Yukawa couplings are given in [3]. The branching ratios are given by

$$BR(h \rightarrow l^\alpha l^\beta) = \frac{\Gamma(h \rightarrow l^\alpha l^\beta)}{\Gamma(h \rightarrow l^\alpha l^\beta) + \Gamma_{SM}} \quad (14)$$

where $l^\alpha, l^\beta = e, \mu, \tau$ and $l^\alpha \neq l^\beta$. The decay width, in turn, is

$$\Gamma(h \rightarrow l^\alpha l^\beta) = \frac{m_h}{8\pi} (|Y_{l^\beta l^\alpha}|^2 + |Y_{l^\alpha l^\beta}|^2) \quad (15)$$

and SM Higgs width is $\Gamma_{SM} = 4.1 \text{ MeV}$ for a 125 GeV Higgs boson. It was assumed that at most one of non-standard decay mode of the Higgs is significant compared to the SM decay width. Figure 26 shows the constraints on the Yukawa couplings derived from the limit $B(H \rightarrow e\tau) < 0.69\%$. This is compared to the constraints from previous indirect measurements. These include a combination of $g - 2$ and EDM searches with marginalization over the complex phases of the Yukawa couplings.

11 Conclusions

The first direct search for Lepton Violating Decays of a Higgs Boson to a electron- τ pair, based on the full 8 TeV dataset collected by CMS in 2012 is presented. The sensitivity of the search is an order of magnitude better than the existing limits. Interpreted as a limit this results in a constraint of $B(H \rightarrow e\tau) < 0.70\%$. The best fit branching fraction is not significantly different from zero but the precision of the measurement still allows a non-null branching fraction for this decay. The limits are subsequently used to constrain $Y_{e\tau}$ Yukawa couplings.

jet category :	0-Jet	1-Jet	2-Jet
Fakes	85.39 ± 14.60	41.61 ± 8.16	2.11 ± 0.96
$Z \rightarrow ee, \mu\mu$	1.10 ± 1.14	4.69 ± 1.30	-
$Z \rightarrow \tau\tau$	86.16 ± 2.93	120.51 ± 8.58	8.34 ± 1.16
$t(\bar{t})$	8.83 ± 1.16	54.96 ± 3.86	11.21 ± 1.18
$t, (\bar{t})$	4.48 ± 0.42	15.80 ± 1.00	2.29 ± 0.24
EWK Diboson	101.99 ± 8.15	66.01 ± 5.18	4.49 ± 0.74
$W\gamma$	0.04 ± 0.04	-	-
$W\gamma^*$	2.42 ± 1.49	0.66 ± 0.59	-
SM Higgs Background, ggf	2.14 ± 0.40	3.30 ± 0.56	0.38 ± 0.17
SM Higgs Background, vbf	0.02 ± 0.01	0.33 ± 0.04	0.80 ± 0.09
Sum of Background	292.56 ± 17.97	307.89 ± 14.24	29.63 ± 2.17
LFV Higgs Signal	33.40 ± 2.32	23.17 ± 1.66	8.57 ± 1.41

Table 17: Event yield in the mass window $100 \text{ GeV} < M_{\text{collinear}} < 150 \text{ GeV}$ for the $H \rightarrow e\tau_\mu$ channel. Both systematics and statistics uncertainties are considered. The expected (pre-fit) contributions are normalized to an integrated luminosity of 19.7 fb^{-1} . The LFV Higgs signal is the MC expectation for $B(H \rightarrow e\tau) = 1\%$. “-” indicates that 0 MC events for the particular background are selected.

Table 18: The expected upper limits on the branching fractions for different jet categories for the $H \rightarrow e\tau$ decay. The one standard-deviation probability intervals around the expected limit are shown in parentheses.

	0 Jet (%)	1 Jet (%)	2 Jets (%)	0-1-2 Jets combined (%)
$e\tau_\mu$	$< 1.63^{(+0.66)}_{(-0.44)}$	$< 1.54^{(+0.71)}_{(-0.47)}$	$< 1.59^{(+0.93)}_{(-0.55)}$	$< 0.85^{(+0.37)}_{(-0.25)}$
$e\tau_{\text{had}}$	$< 2.71^{(+1.05)}_{(-0.75)}$	$< 2.76^{(+1.07)}_{(-0.77)}$	$< 3.55^{(+1.38)}_{(-0.99)}$	$< 1.73^{(+1.01)}_{(-0.48)}$
$e\tau$			$< 0.75^{(+0.32)}_{(-0.22)}$	

References

- [1] J. D. Bjorken and S. Weinberg, “Mechanism for Nonconservation of Muon Number”, *Phys. Rev. Lett.* **38** (Mar, 1977) 622–625, doi:[10.1103/PhysRevLett.38.622](https://doi.org/10.1103/PhysRevLett.38.622).
- [2] G. Blankenburg, J. Ellis, and G. Isidori, “Flavour-Changing Decays of a 125 GeV Higgs-like Particle”, *Phys.Lett.* **B712** (2012) 386–390, doi:[10.1016/j.physletb.2012.05.007](https://doi.org/10.1016/j.physletb.2012.05.007), arXiv:[1202.5704](https://arxiv.org/abs/1202.5704).
- [3] R. Harnik, J. Kopp, and J. Zupan, “Flavor Violating Higgs Decays”, *JHEP* **1303** (2013) 026, doi:[10.1007/JHEP03\(2013\)026](https://doi.org/10.1007/JHEP03(2013)026), arXiv:[1209.1397](https://arxiv.org/abs/1209.1397).
- [4] D. Troedle et al., “Search for Lepton Flavour Violating Decays of the Higgs Boson”, CMS Analysis Note 2013/244, 2014.
- [5] CMS Collaboration Collaboration, “Evidence for the 125 GeV Higgs boson decaying to a pair of τ leptons”, arXiv:[1401.5041](https://arxiv.org/abs/1401.5041).
- [6] CMS Collaboration Collaboration, “Search for neutral Higgs bosons decaying to τ pairs in pp collisions at $\sqrt{s} = 7 \text{ TeV}$ ”, *Phys.Lett.* **B713** (2012) 68–90, doi:[10.1016/j.physletb.2012.05.028](https://doi.org/10.1016/j.physletb.2012.05.028), arXiv:[1202.4083](https://arxiv.org/abs/1202.4083).

Table 19: The observed upper limits on the branching fractions for the $H \rightarrow e\tau$ decay and different event categories .

	0 Jet (%)	1 Jet (%)	2 Jets (%)	0-1-2 Jets combined (%)
$e\tau_\mu$	< 1.83	< 0.94	< 1.49	< 0.74
$e\tau_{had}$	< 3.92	< 3.00	< 2.88	< 2.01
$e\tau$			< 0.69	

Table 20: The best fit values for the branching fractions for different jet categories for the $H \rightarrow e\tau$ decay.

	0 Jet (%)	1 Jet (%)	2 Jets (%)	0-1-2 Jets combined (%)
$e\tau_\mu$	$0.19^{+0.85}_{-0.85}$	$-1.04^{+0.70}_{-0.70}$	$-0.12^{+0.67}_{-0.58}$	$-0.17^{+0.41}_{-0.40}$
$e\tau_{had}$	$1.43^{+1.38}_{-1.33}$	$0.30^{+1.37}_{-1.38}$	$-0.91^{+1.54}_{-1.57}$	$0.31^{+0.91}_{-0.88}$
$e\tau$			$-0.10^{+0.37}_{-0.36}$	

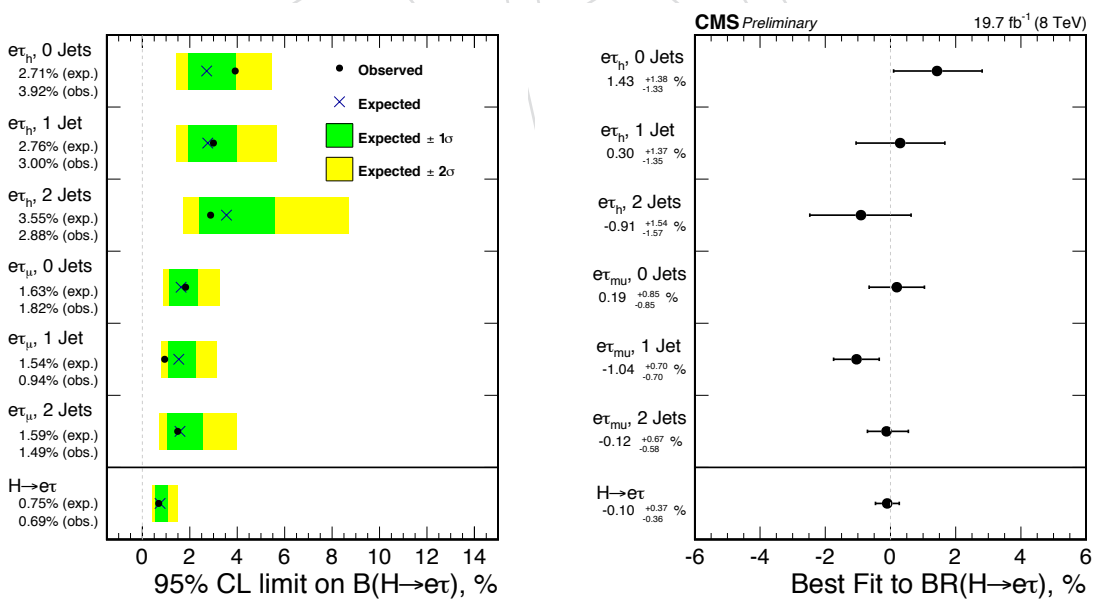


Figure 25: Left) Limits by Category for LFV $H \rightarrow e\tau$ decays. Right) Best fit branching fractions by category.

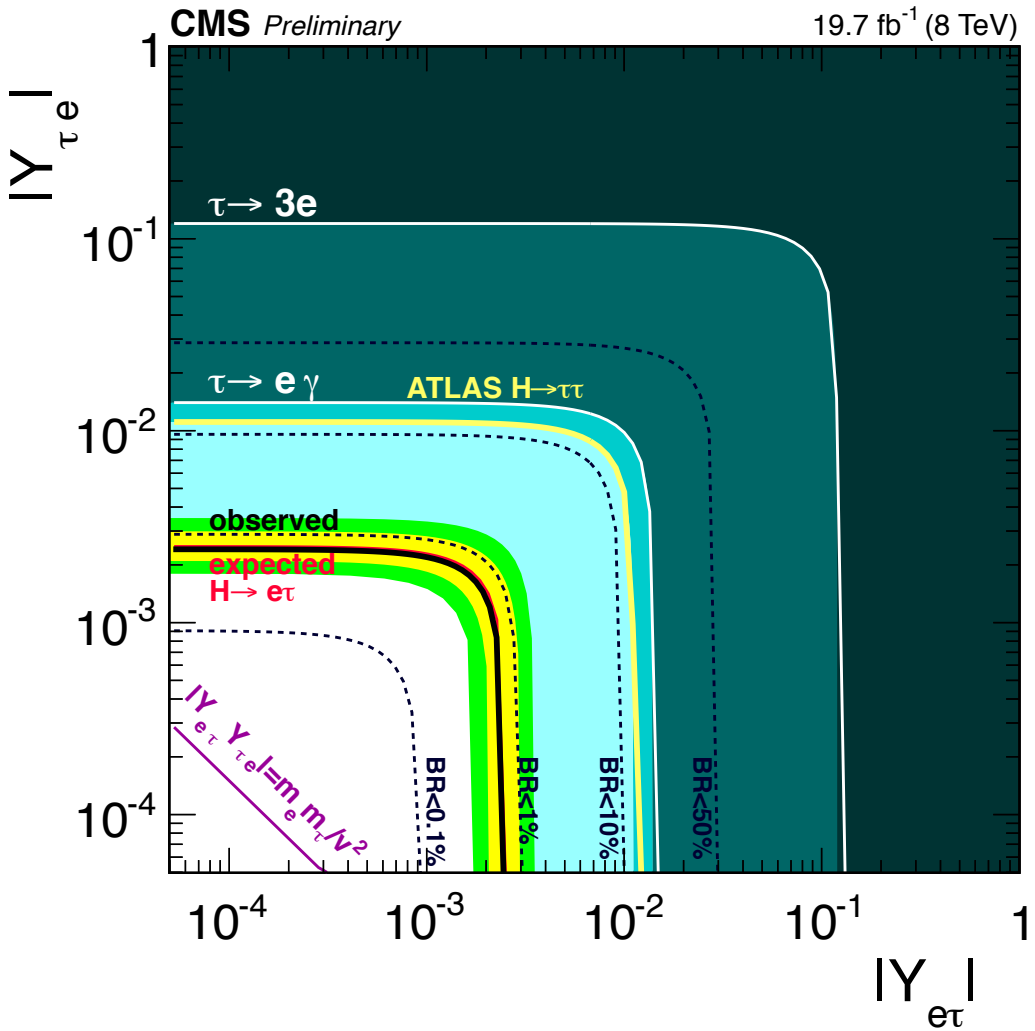


Figure 26: Constraints on the flavor violating Yukawa couplings, $|Y_{e\tau}|, |Y_{\tau e}|$. The expected(red solid line) and observed(black solid line) limits are derived from the limit on $B(H \rightarrow e\tau)$ from the present analysis. The diagonal Yukawa couplings are approximated by their SM values. The black dashed lines are contours of $B(H \rightarrow e\tau)$ for reference. The shaded regions are derived constraints from null searches for $\tau \rightarrow 3e$ (dark green) and $\tau \rightarrow e\gamma$ (lighter green). The thin red dotted line is the theoretical naturalness limits $Y_{ij}Y_{ji} \leq m_i m_j / v^2$. The yellow line is the limit from a re-interpretation, by a theoretical group [3], of an ATLAS $H \rightarrow \tau\tau$ search

jet category :	0-Jet	1-Jet	2-Jet
Fakes	6005.55 ± 41.38	546.16 ± 17.86	30.53 ± 3.97
$Z \rightarrow ee, \mu\mu$	1001.96 ± 38.36	165.09 ± 5.03	11.70 ± 0.44
$Z \rightarrow \tau\tau$	497.50 ± 12.69	209.21 ± 12.98	23.93 ± 3.59
$t\bar{t}$	18.50 ± 0.87	25.08 ± 1.03	2.31 ± 0.32
t, \bar{t}	32.26 ± 5.61	37.74 ± 5.63	-
EWK Diboson	132.06 ± 2.65	20.52 ± 0.42	1.16 ± 0.05
SM Higgs Background, ggf	14.89 ± 0.77	4.82 ± 0.25	0.44 ± 0.07
SM Higgs Background, vbf	0.22 ± 0.04	0.79 ± 0.06	1.74 ± 0.13
Sum of Background	7702.94 ± 43.65	1009.40 ± 20.66	71.82 ± 5.31
LFV Higgs Signal	0.00 ± 0.23	0.00 ± 0.06	0.00 ± 0.01

Table 21: Event yield in the extended mass window $50 \text{ GeV} < M_{\text{collinear}} < 300 \text{ GeV}$ for the $H \rightarrow e\tau_{\text{had}}$ channel estimated from the fit. Both systematics and statistics uncertainties are considered. The contributions are normalized to an integrated luminosity of 19.7 fb^{-1} .

jet category :	0-Jet	1-Jet	2-Jet
Fakes	3366.35 ± 25.05	223.46 ± 10.74	8.73 ± 2.23
$Z \rightarrow ee, \mu\mu$	713.91 ± 29.63	84.84 ± 3.68	3.16 ± 0.25
$Z \rightarrow \tau\tau$	269.79 ± 9.86	32.31 ± 3.45	1.62 ± 0.30
$t(\bar{t})$	5.03 ± 0.44	6.06 ± 0.53	0.50 ± 0.15
$t, (\bar{t})$	4.91 ± 1.88	7.11 ± 2.43	-
EWK Diboson	52.68 ± 1.97	6.31 ± 0.24	0.28 ± 0.03
SM Higgs Background, ggf	11.92 ± 0.72	2.86 ± 0.21	0.27 ± 0.06
SM Higgs Background, vbf	0.17 ± 0.04	0.43 ± 0.03	0.74 ± 0.07
Sum of Background	4424.76 ± 27.59	363.39 ± 10.89	15.30 ± 2.27
LFV Higgs Signal	0.00 ± 0.23	0.00 ± 0.06	0.00 ± 0.01

Table 22: Event yield in the mass window $100 \text{ GeV} < M_{\text{collinear}} < 150 \text{ GeV}$ for the $H \rightarrow e\tau_{\text{had}}$ channel estimated from the fit. Both systematic and statistic uncertainties are considered. The contributions are normalized to an integrated luminosity of 19.7 fb^{-1} .

- 516 [7] CMS Collaboration Collaboration, “Performance of tau-lepton reconstruction and
517 identification in CMS”, *JINST* **7** (2012) P01001,
518 doi:10.1088/1748-0221/7/01/P01001, arXiv:1109.6034.
- 519 [8] A. Apyan et al., “Physics Objects in the Higgs to tau tau Analysis”, CMS Analysis Note
520 2013/188, 2013.
- 521 [9] CMS Collaboration, “Search for Lepton Flavour Violating Decays of the Higgs Boson”,
522 (2014). CMS AN-2013/244.
- 523 [10] CMS Collaboration, “Search for Lepton Flavour Violating Decays of the Higgs Boson”,
524 (2014). CMS-PAS-HIG-14-005.
- 525 [11] CMS Collaboration, “Search for lepton-flavour-violating decays of the Higgs boson”,
526 (2015). arXiv:1502.07400. Submitted to *Phys. Lett. B*.
- 527 [12] T. Sjöstrand, S. Mrenna, and P. Skands, “A Brief Introduction to PYTHIA 8.1”, (2007)
528 arXiv:0710.3820.

jet category :	0-Jet	1-Jet	2-Jet
Fakes	163.93 ± 8.24	86.07 ± 6.08	9.87 ± 1.49
$Z \rightarrow ee, \mu\mu$	2.50 ± 0.81	7.24 ± 0.54	0.00 ± 0.00
$Z \rightarrow \tau\tau$	168.83 ± 3.01	415.07 ± 8.60	44.15 ± 1.86
$t\bar{t}$	56.63 ± 1.84	205.85 ± 4.14	37.18 ± 1.44
t, \bar{t}	24.39 ± 0.76	51.89 ± 1.34	6.49 ± 0.27
EWK Diboson	279.54 ± 4.97	149.82 ± 3.17	10.85 ± 0.67
$W\gamma$	1.75 ± 1.36	-	-
$W\gamma^*$	6.30 ± 1.88	1.18 ± 0.60	0.05 ± 0.03
SM Higgs Background, ggf	3.00 ± 0.36	4.39 ± 0.44	0.46 ± 0.15
SM Higgs Background, vbf	0.03 ± 0.01	0.46 ± 0.03	1.23 ± 0.07
Sum of Background	706.90 ± 9.30	921.96 ± 11.03	110.27 ± 2.86
LFV Higgs Signal	0.00 ± 0.09	0.00 ± 0.07	0.00 ± 0.03

Table 23: Event yield in the mass window $50 \text{ GeV} < M_{\text{collinear}} < 300 \text{ GeV}$ for the $H \rightarrow e\tau_\mu$ channel estimated from the fit. Both systematics and statistics uncertainties are considered. The contributions are normalized to an integrated luminosity of 19.7 fb^{-1} . “-” indicates that 0 MC events for the particular background are selected.

jet category :	0-Jet	1-Jet	2-Jet
Fakes	85.15 ± 5.91	38.11 ± 3.86	2.10 ± 0.67
$Z \rightarrow ee, \mu\mu$	2.28 ± 0.60	5.37 ± 0.51	-
$Z \rightarrow \tau\tau$	84.72 ± 2.11	113.32 ± 4.20	8.54 ± 0.63
$t(\bar{t})$	9.44 ± 0.72	54.55 ± 2.22	10.64 ± 0.79
$t, (\bar{t})$	4.36 ± 0.30	14.85 ± 0.77	2.05 ± 0.16
EWK Diboson	83.00 ± 2.67	51.65 ± 2.01	3.57 ± 0.37
$W\gamma$	0.04 ± 0.03	-	-
$W\gamma^*$	2.17 ± 1.03	0.56 ± 0.39	-
SM Higgs Background, ggf	2.30 ± 0.31	3.26 ± 0.39	0.38 ± 0.14
SM Higgs Background, vbf	0.02 ± 0.01	0.33 ± 0.03	0.76 ± 0.06
Sum of Background	273.48 ± 6.12	282.00 ± 5.96	28.05 ± 1.33
LFV Higgs Signal	0.00 ± 0.09	0.00 ± 0.06	0.00 ± 0.03

Table 24: Event yield in the mass window $100 \text{ GeV} < M_{\text{collinear}} < 150 \text{ GeV}$ for the $H \rightarrow e\tau_\mu$ channel estimated from the fit. Both systematics and statistics uncertainties are considered. The contributions are normalized to an integrated luminosity of 19.7 fb^{-1} . “-” indicates that 0 MC events for the particular background are selected.

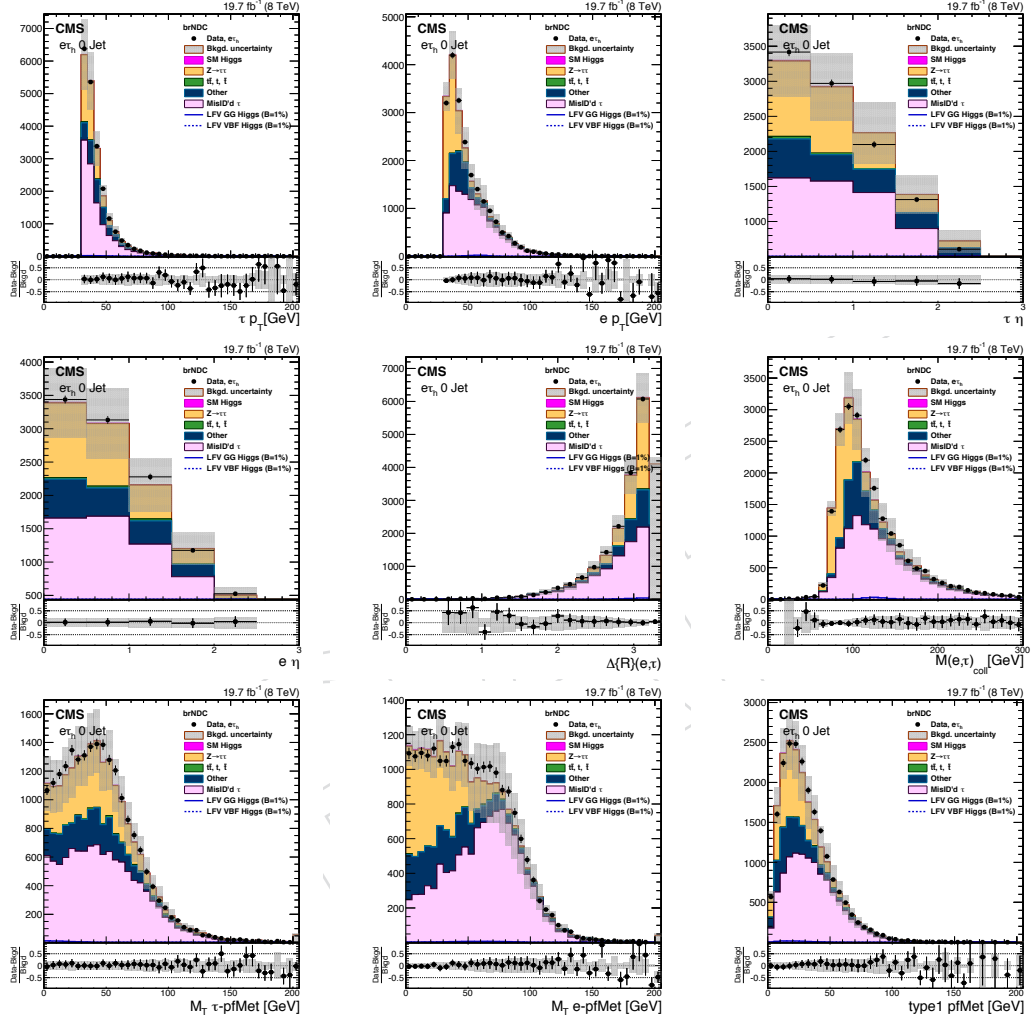
- 529 [13] CMS Collaboration, “Particle–Flow Event Reconstruction in CMS and Performance for
530 Jets, Taus, and E_T^{miss} ”, CMS Physics Analysis Summary CMS-PAS-PFT-09-001, 2009.
531 [14] CMS Collaboration, “Commissioning of the Particle-flow Event Reconstruction in
532 Minimum-Bias and Jet Events from pp Collisions at 7 TeV”, CMS Physics Analysis
533 Summary CMS-PAS-PFT-10-002, 2010.
534 [15] CMS Collaboration, “Commissioning of the particle–flow event reconstruction with
535 leptons from J/ψ and W decays at 7 TeV”, CMS Physics Analysis Summary
536 CMS-PAS-PFT-10-003, 2010.
537 [16] K. Rose, “Deterministic Annealing for Clustering, Compression, Classification,

- 538 Regression and related Optimisation Problems”, *Proceedings of the IEEE* **Vol. 86, Issue 11**
539 (1998).
- 540 [17] M. Cacciari, G. P. Salam, and G. Soyez, “The anti- k_t jet clustering algorithm”, *JHEP* **04**
541 (2008) 063, doi:10.1088/1126-6708/2008/04/063, arXiv:0802.1189.
- 542 [18] M. Cacciari, G. P. Salam, “Dispelling the N^3 myth for the k_t jet-finder”, *Phys. Lett. B* **641**
543 (2006) 57, doi:10.1016/j.physletb.2006.08.037, arXiv:hep-ph/0512210.
- 544 [19] CMS Collaboration, “Determination of jet energy calibration and transverse momentum
545 resolution in CMS”, *JINST* **6** (2011) 11002, doi:10.1088/1748-0221/6/11/P11002,
546 arXiv:1107.4277.
- 547 [20] A. Hoecker et al., “TMVA - toolkit for multivariate data analysis”, arXiv:0703039.
- 548 [21] CMS Collaboration, “Identification of b-quark jets with the CMS experiment”, *CMS*
549 *Physics Analysis Summary CMS-PAS-BTV-12-001* (2012).
- 550 [22] CMS Collaboration, “Performance of tau-lepton reconstruction and identification in
551 CMS”, *JINST* **7** (2012) P01001, doi:10.1088/1748-0221/7/01/P01001.
- 552 [23] R. K. Ellis, I. Hinchliffe, M. Soldate, and J. van der Bij, “Higgs Decay to tau+ tau-: A
553 Possible Signature of Intermediate Mass Higgs Bosons at the SSC”, *Nucl.Phys.* **B297**
554 (1988) 221, doi:10.1016/0550-3213(88)90019-3.
- 555 [24]
556 <https://twiki.cern.ch/twiki/bin/viewauth/CMS/SWGuideHiggsAnalysisCombinedLimit>.
- 557 [25] T. F. A. Burgmeier and C. Veelken, “Modelling backgrounds via Embedding technique
558 applied on recHit level”, CMS Analysis Note 2013/073, 2013.
- 559 [26] V. Chiochia et al., “Estimation of tau efficiency in 7 TeV data”, CMS Analysis Note
560 2011/200, 2011.
- 561 [27] M. Chen et al., “Estimation of tau efficiency in 8 TeV data”, CMS Analysis Note 2011/514,
562 2011.
- 563 [28] P. Nadolsky et al., “Implications of CTEQ global analysis for collider observables”, *Phys.*
564 *Rev. D* **78** (2008) arXiv:0802.0007.
- 565 [29] A. D. Martin et al., “Parton distributions for the LHC”, *Eur. Phys. J. C* **63** (2009)
566 doi:10.1140/epjc/s10052-009-1072-5, arXiv:0901.0002.
- 567 [30] NNPDF Collaboration, “A first unbiased global NLO determination of parton
568 distributions and their uncertainties”, *Nucl. Phys. B* **838** (2010)
569 doi:10.1016/j.nuclphysb.2010.05.008, arXiv:1002.4407.
- 570 [31] M. Botje et al., “The PDF4LHC Working Group Interim Recommendations”,
571 arXiv:1101.0538.
- 572 [32] C. Collaboration, “Jet Energy Corrections and Uncertainties for 2012”, CMS DP 2012/012,
573 2012.

574 A Control plots after preselection

575 A.1 $e\tau_{had}$ channel

576 Figures 27, 28, and 29 show the measured and expected kinematic distributions after preselection cuts for the 0-jet, 1-jet and 2-jet categories, respectively. The shaded bands represent the
 577 quadratic sum of the systematic uncertainties discussed in Section 8. Background expectations
 578 are evaluated with MC simulation and data-driven techniques as described in Section 6.



579 Figure 27: Measured and expected kinematic distributions of the $e\tau_{had}$ channel after preselection cuts for the 0-jet category. From left to right and top to bottom: τ p_T , electron p_T , τ pseudorapidity, electron pseudorapidity, ΔR separation between electron and τ , collinear mass, transverse mass of τ and PFMET, transverse mass of electron and PFMET, and PFMET.

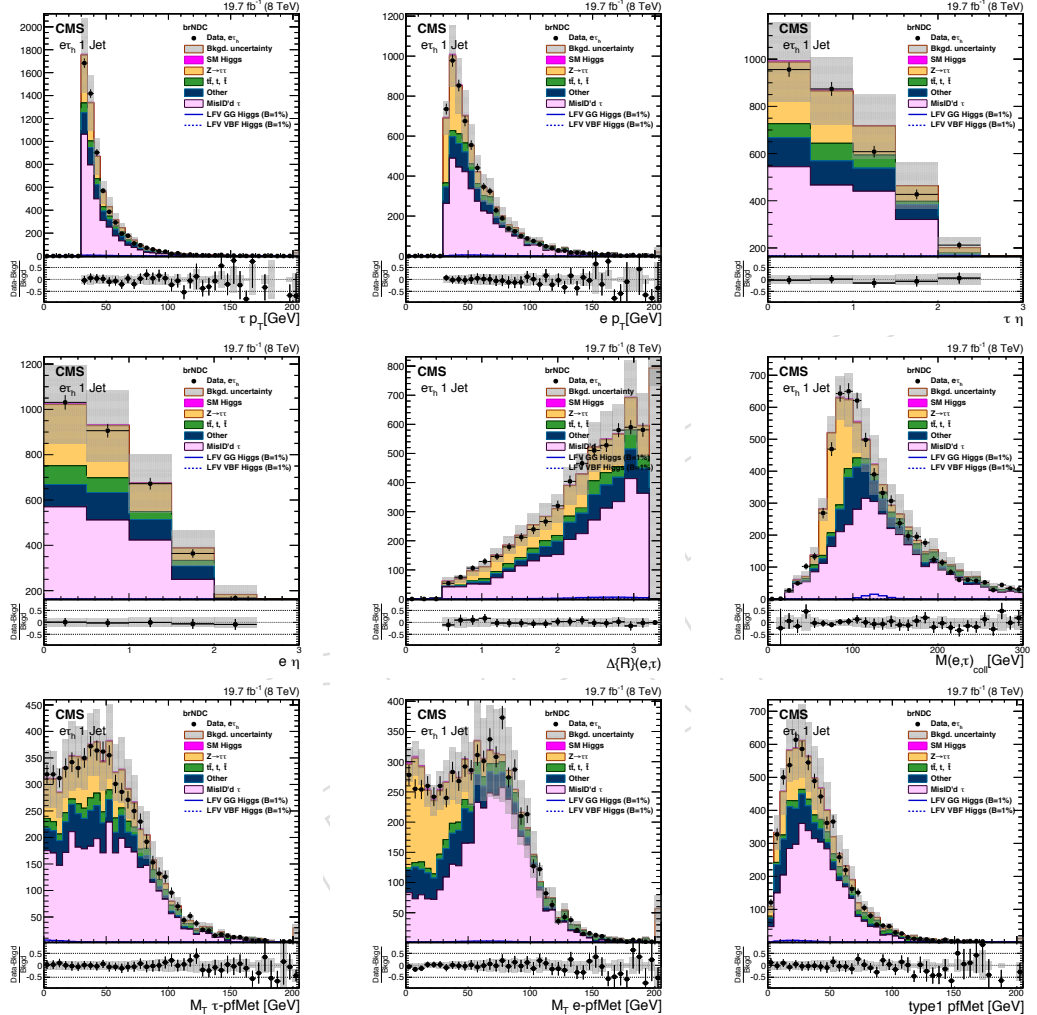


Figure 28: Measured and expected kinematic distributions of the $e\tau_{had}$ channel after preselection cuts for the 1-jet category. From left to right and top to bottom: τp_T , electron p_T , τ pseudorapidity, electron pseudorapidity, ΔR separation between electron and τ , collinear mass, transverse mass of τ and PFMET, transverse mass of electron and PFMET, and PFMET.

A Control plots after preselection

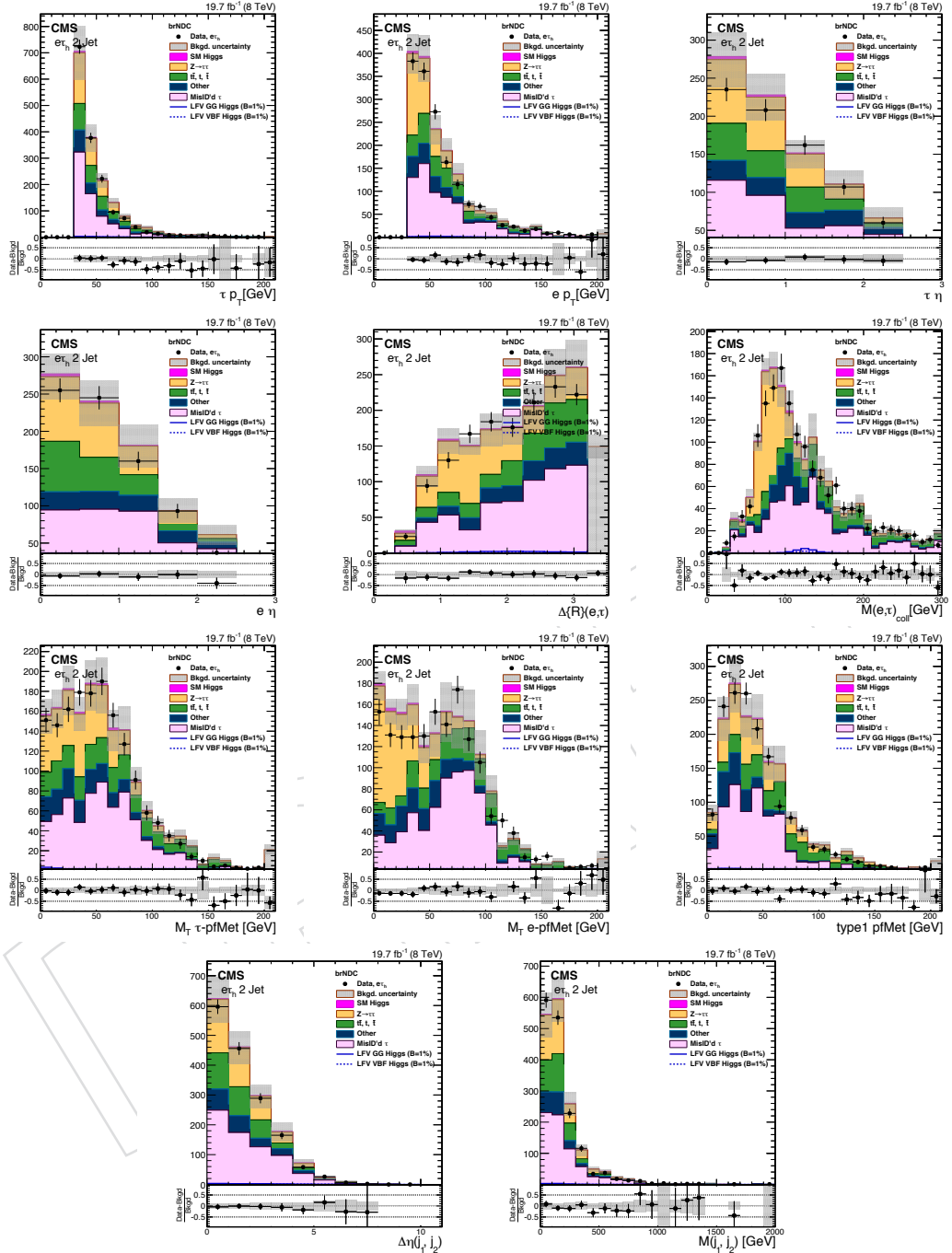


Figure 29: Measured and expected kinematic distributions of the $e\tau_{had}$ channel after preselection cuts for the 2-jet category. From left to right and top to bottom: τp_T , electron p_T , τ pseudorapidity, electron pseudorapidity, ΔR separation between electron and τ , collinear mass, transverse mass of τ and PFMET, transverse mass of electron and PFMET, PFMET, difference in pseudorapidity of the two jets, and the dijet mass.

580 A.2 $e\tau_\mu$ channel

581 Figures 30, 31, and 32 show the measured and expected kinematic distributions after preselection cuts for the 0-jet, 1-jet and 2-jet categories, respectively. Background expectations are
 582 evaluated with MC simulation and data-driven techniques as described in Section 6.
 583

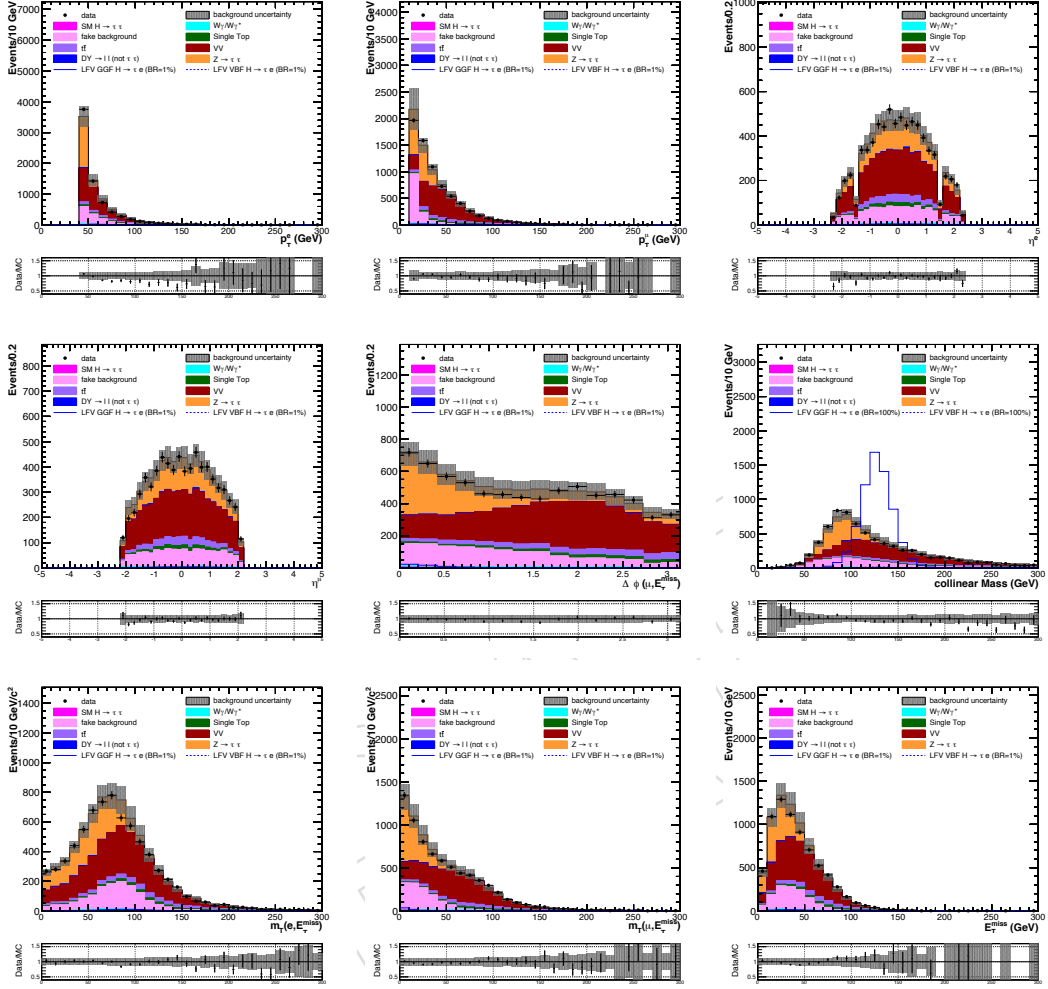


Figure 30: Measured and expected kinematic distributions of the $e\tau_\mu$ channel after preselection cuts for the 0-jet category. From left to right and top to bottom: electron p_T , muon p_T , electron pseudorapidity, muon pseudorapidity, $\Delta\Phi$ separation between electron and MET, collinear mass, transverse mass of electron and PFMET, transverse mass of muon and PFMET, and PFMET.

A Control plots after preselection

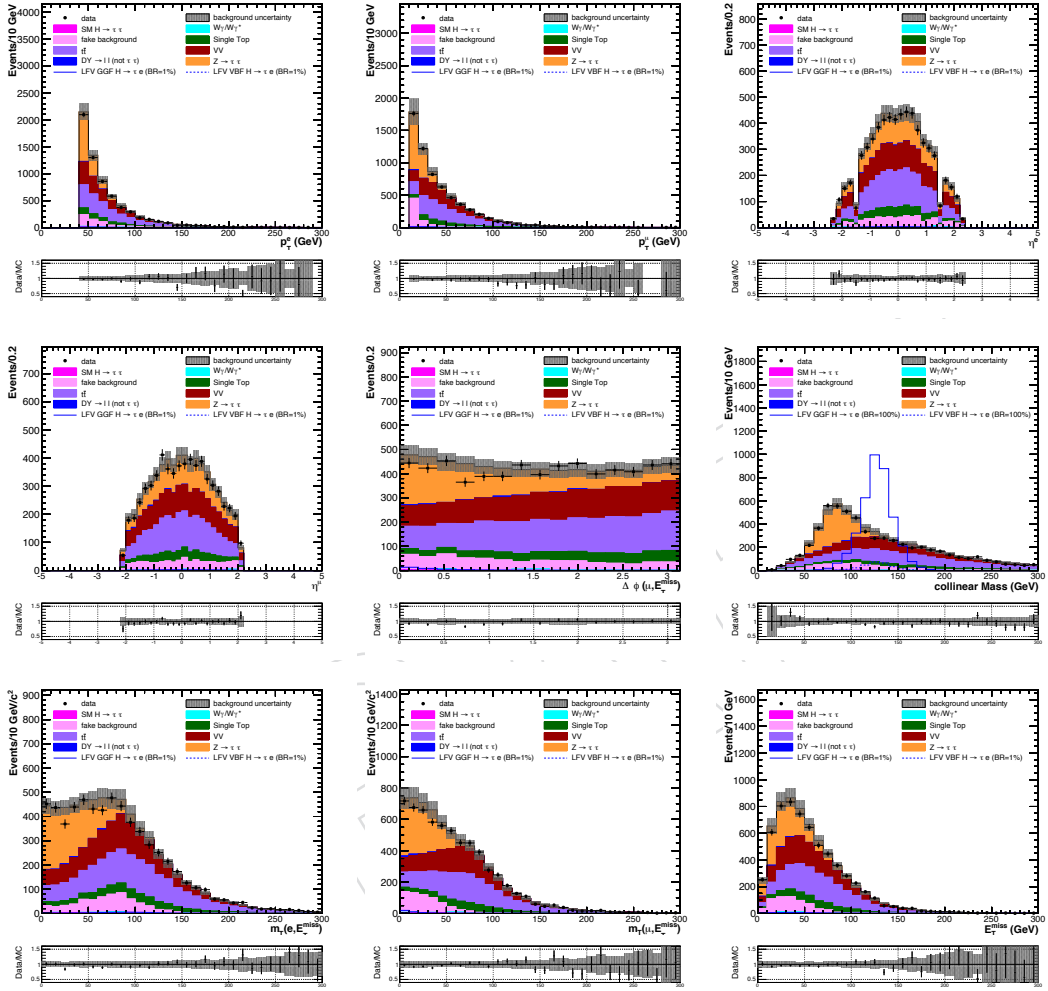


Figure 31: Measured and expected kinematic distributions of the $e\tau_\mu$ channel after preselection cuts for the 1-jet category. From left to right and top to bottom: electron p_T , muon p_T , electron pseudorapidity, muon pseudorapidity, $\Delta\Phi$ separation between electron and MET, collinear mass, transverse mass of electron and PFMET, transverse mass of muon and PFMET, and PFMET

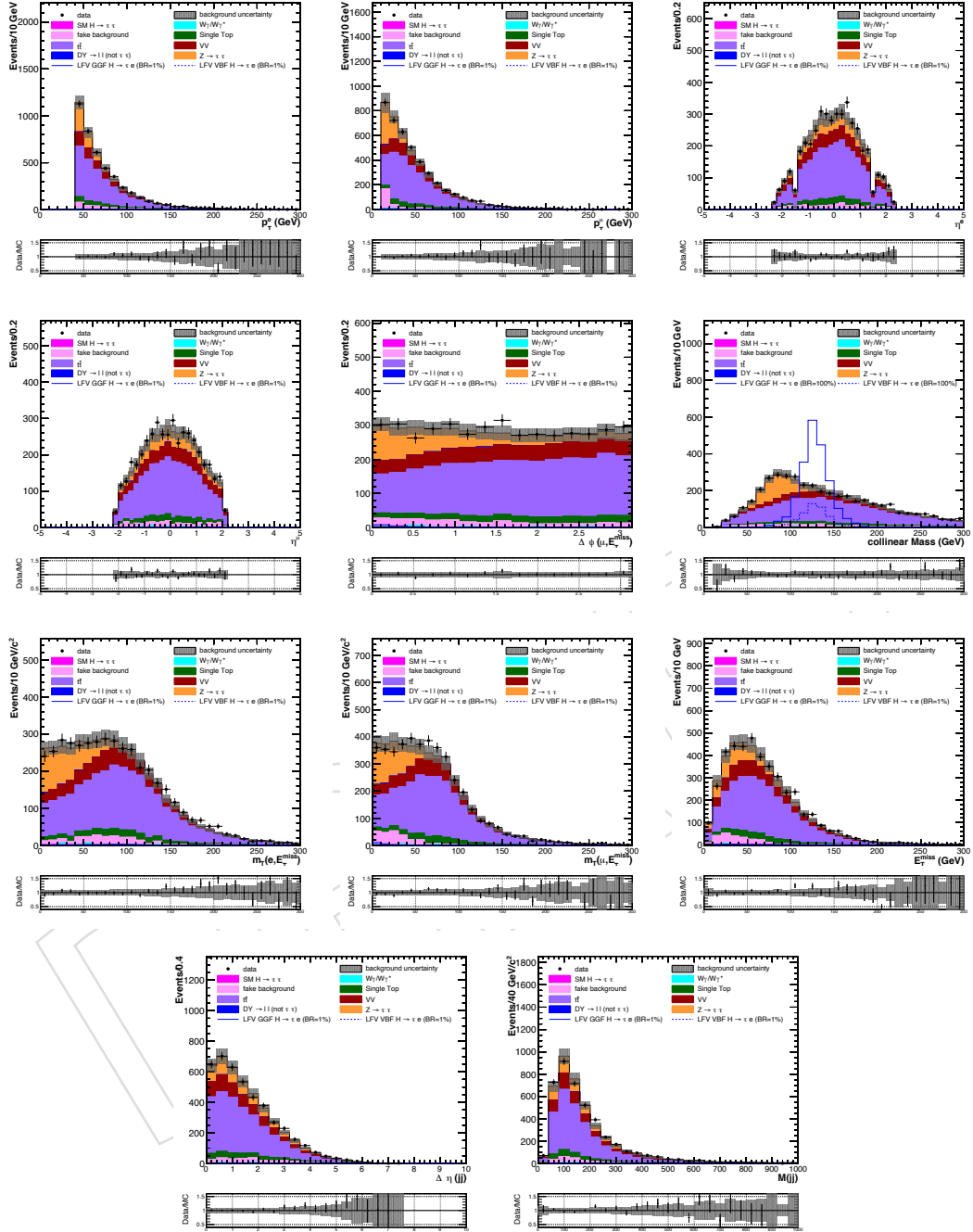


Figure 32: Measured and expected kinematic distributions of the $e\tau_\mu$ channel after preselection cuts for the 2-jet category. From left to right and top to bottom: electron p_T , muon p_T , electron pseudorapidity, muon pseudorapidity, $\Delta\Phi$ separation between electron and MET, collinear mass, transverse mass of electron and PFMET, transverse mass of muon and PFMET, PFMET, difference in pseudorapidity of the two jets, and the dijet mass.

584 **A.3 $e\tau_\mu$ channel: shape systematics**

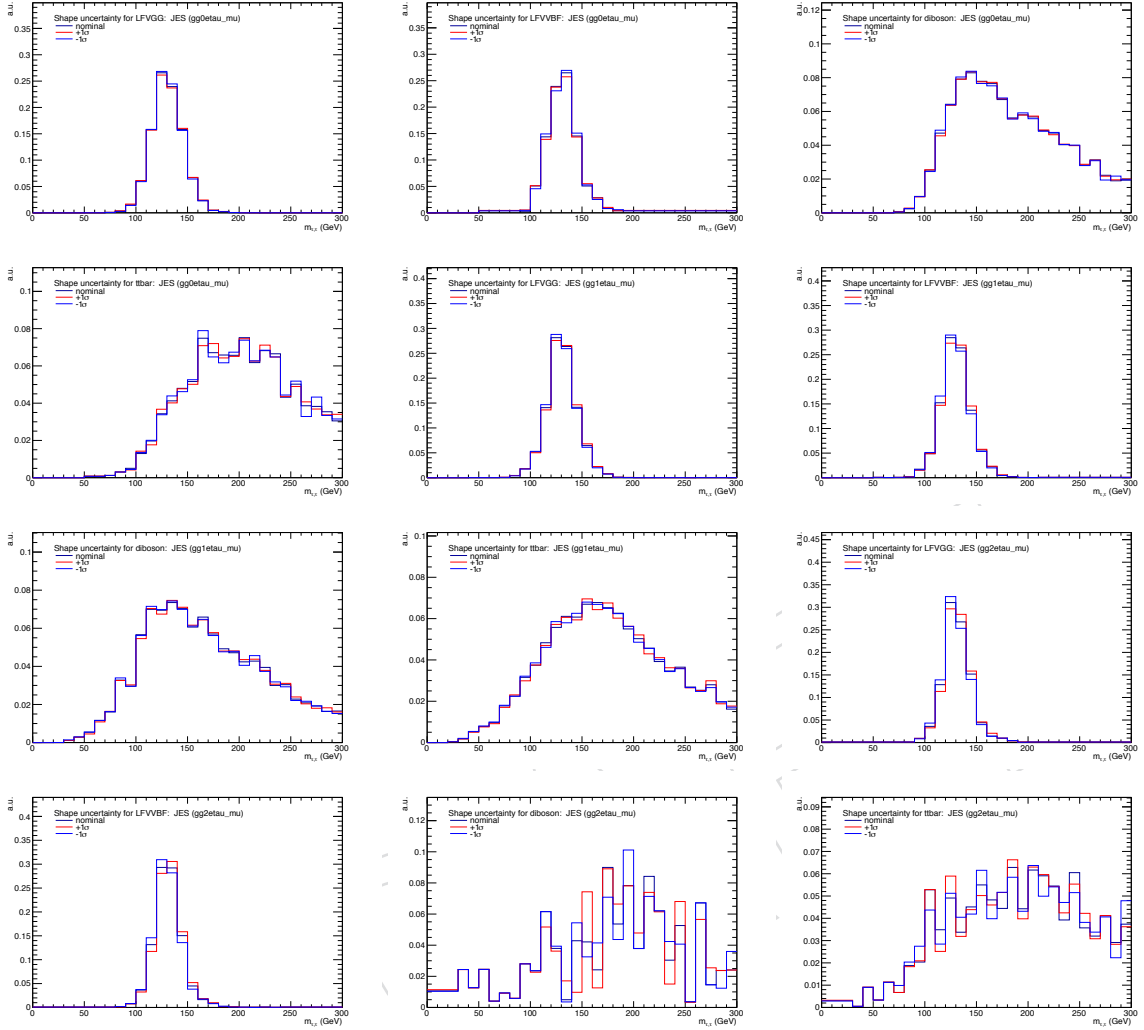


Figure 33: Shape systematic templates associated to the JES uncertainty for the signal (LFVGG,LFVVBF) and major backgrounds(diboson,ttbar). The collinear mass distributions in the jet categories 0-jet,1-jet and 2-jet, after all selection, are shown for the $H \rightarrow e\tau_\mu$ channel.

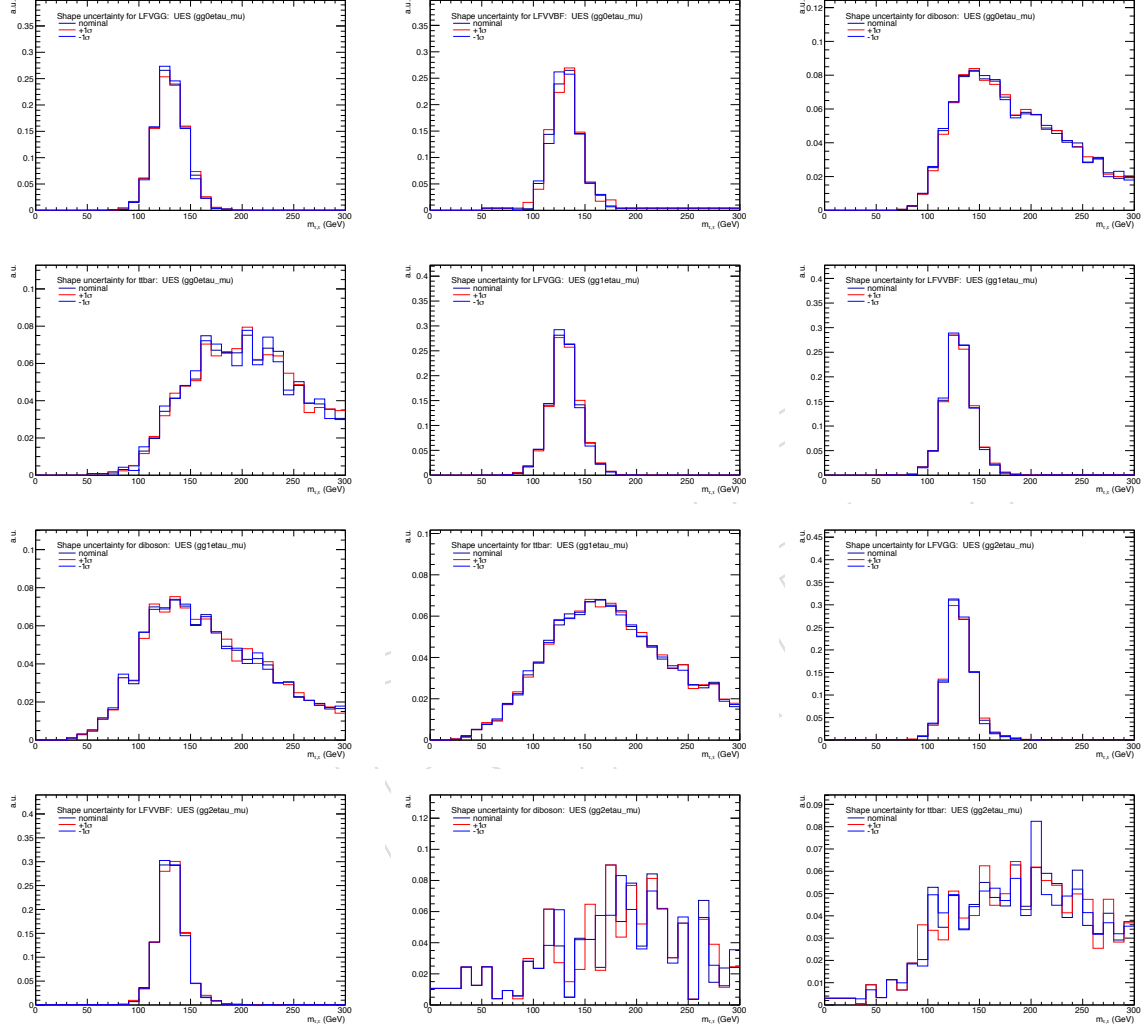


Figure 34: Shape systematic templates associated to the unclustered energy uncertainty for the signal (LFVGG,LFVVBF) and major backgrounds(diboson,ttbar). The collinear mass distributions in the jet categories 0-jet,1-jet and 2-jet, after all selection, are shown for the $H \rightarrow e\tau_\mu$ channel.

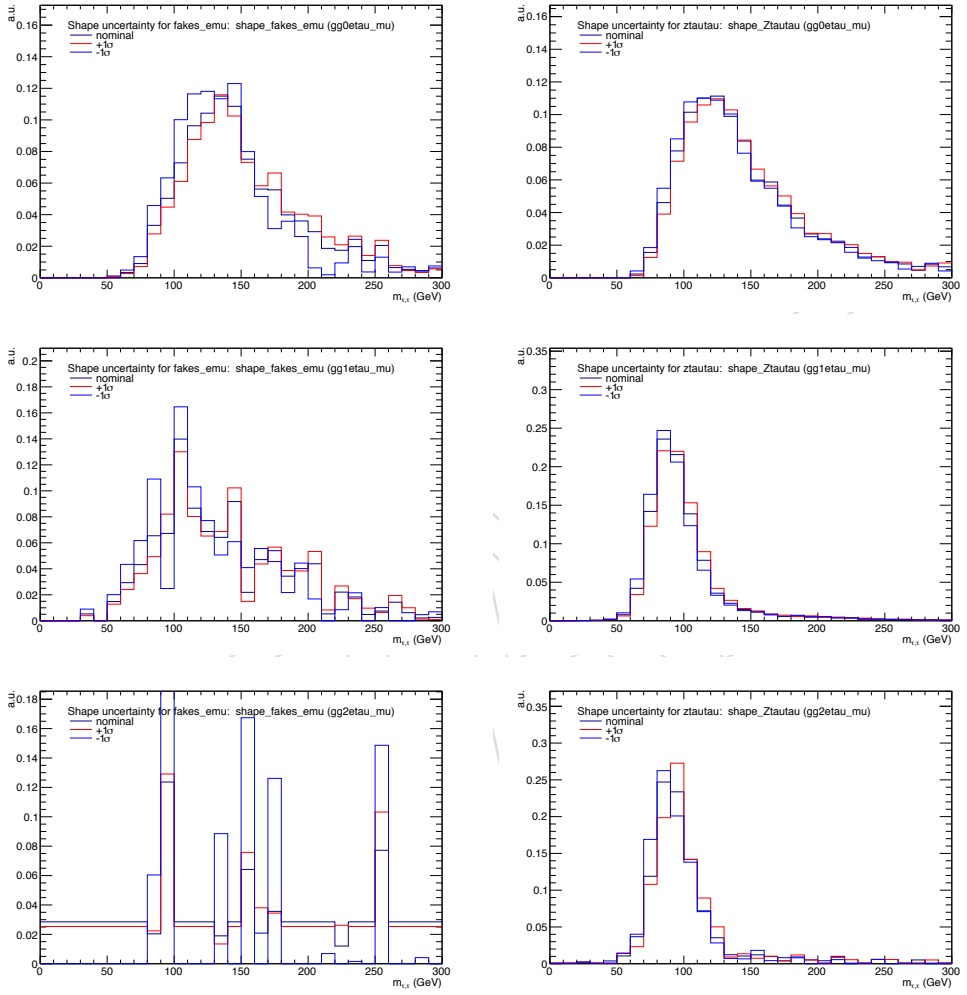


Figure 35: Shape systematic templates associated to the Ztautau bias corrections and the fake rate uncertainty. The collinear mass distributions in the jet categories 0-jet, 1-jet and 2-jet, after all selection, are shown for the $H \rightarrow e\tau_\mu$ channel.